NEAR-INFRARED SUBARCSECOND OBSERVATIONS OF ULTRACOMPACT H II REGIONS[1]

CARLOS ALVAREZ, MARKUS FELDT, THOMAS HENNING, ELENA PUGA, AND WOLFGANG BRANDNER

Max-Planck-Institut für Astronomie, Königstuhl 17, D-69117 Heidelberg, Germany

AND

BRINGFRIED STECKLUM

Thüringer Landessternwarte Tautenburg, Sternwarte 5, D-07778 Tautenburg, Germany

ABSTRACT

We present adaptive optics (AO) assisted *J*, *H*, and *K/K′* images of eight ultracompact H II (UC H II) regions taken with the ALFA and ADONIS AO systems at Calar Alto and La Silla observatories. The images show details of the stellar population and the near-IR morphology of UC H II regions with unprecedented resolution. We have searched for the ionizing sources of the regions using near-IR photometry. The spectral type of the ionizing and most luminous stars inferred from our photometry has been compared with spectral type estimates from *IRAS* and published radio-continuum measurements. We find that the photometric near-IR spectral types are earlier than estimates from radio and *IRAS* data. This difference is alleviated when stellar spherical models including line blanketing and stellar winds instead of non-LTE plane-parallel models are used to derive the radio- and *IRAS*-based spectral types. We also made an attempt to correlate the properties of the near-IR ionizing population with *MSX* data and published CS measurements. No correlation was found. We note that in two of the regions (G309.92+0.48 and G61.48+0.09B1), the best candidate to ionize the region is possibly a supergiant.

Subject headings: catalogs — H II regions — infrared: ISM — instrumentation: adaptive optics — techniques: high angular resolution

Online material: color figures

1. INTRODUCTION

The formation of massive stars ($M \geq 8\,M_\odot$) is a major open problem in astrophysics. In contrast to the formation of low-mass stars, the Kelvin-Helmholtz timescale for the onset of nuclear fusion within massive protostars is shorter than the accretion timescale. In other words, massive stars reach the zero-age main sequence (ZAMS) while still being embedded in their natal molecular clouds. It is commonly argued that during this phase the radiation pressure is so high that it can substantially decrease or even halt the infall (e.g., Wolfire & Cassinelli 1987). However, this scenario contradicts the existence of stars with masses up to $100\,M_\odot$.

Quite a number of loopholes from this dilemma have been proposed: mass build-up through disk accretion (e.g., McKee & Tan 2002; Yorke & Sonnhalter 2002), accretion with extremely large (e.g., Nakano et al. 2000) or increasing (e.g., Behrend & Maeder 2001) infall rates, or—as a completely different approach—coalescence of less massive stars in young and dense cluster environments (Bonnell et al. 1998). Each model provides specific predictions that, in principle, can be tested observationally, e.g., the presence of accretion disks, the existence of relations in the infall-outflow dynamics, or an enhanced binarity/multiplicity frequency.

Observationally, however, we still know little about the early stages of massive star formation. Massive stars are rare and hence statistically located at larger distances than sites of low-mass star formation. Additionally, massive stars tend to form in clusters and associations. They have a strong impact on their environment producing outflows, large and bright ionized regions, clumps of heated dust, and reflection nebulae. To disentangle these complex, far-away regions, very high sensitivity and resolution are required. Moreover, the natal molecular clouds these objects are still embedded in produce tens to hundreds of magnitudes of visual extinction, which makes them accessible only at long wavelengths.

To overcome these observational limitations, early surveys of sites of massive star formation focused on using the Very Large Array (VLA) to detect the radio continuum emitted from so-called ultracompact H II (UC H II) regions. UC H II regions represent a relatively evolved phase in the young massive star's life, when it has already ionized a substantial amount of surrounding gas (e.g., Wood & Churchwell 1989). For long years, this was the earliest phase of massive stars' lifes accessible to astronomers, and only at wavelengths longer than 1 mm.

Only in recent years have adaptive optics (AO) systems working in the near-infrared (NIR) provided high enough resolution to start disentangling individual stars. At these wavelengths, the visual extinction toward some of the embedded central ionizing stars can *just* be overcome. AO-assisted imaging of this kind allowed the identification of the ionizing objects and the stellar content in a number of sites of massive star formation (Feldt et al. 1998, 1999; Henning et al. 2001, 2002).

In this paper, we present the results of a mini survey of AO-assisted NIR observations toward eight UC H II regions. The sample (see Table 1) was selected from the catalogs of Bronfman et al. (1996), Wood & Churchwell (1989), and Kurtz et al. (1994). All sources are located within 30″ of a bright optical star to be used as wavefront sensor reference for the AO observations. We present the photometry of sources found to be embedded in or close to the known sites of massive star

---

TABLE 1

Target List

Object (1)	IRAS Name (2)	α[a] (3)	δ[a] (4)	l (deg)[b] (5)	b (deg)[b] (6)	Reference[c] (7)	Type[d] (8)	Other Names (9)
G309.92+0.48	13471−6120	13 50 41.8	−61 35 11	309.92	0.48	1, 2, 6, 8	UN	GL 4182
G351.16+0.70[e]	17165−3554	17 19 58.2	−35 57 32	351.16	0.70	1, 3, 6, 8	...	NGC 6334V
G5.89−0.39..........	17574−2403	18 00 30.4	−24 04 00	5.89	−0.40	2, 3, 5, 6, 8, 11	SH	W28 A2
G11.11−0.40........	18085−1931	18 11 33.2	−19 30 39	11.11	−0.40	2, 9, 12	IR	...
G18.15−0.28........	18222−1317	18 25 01.0	−13 15 40	18.15	−0.29	2, 3, 9, 12	CO	...
G61.48+0.09[f]	19446+2505	19 46 46.6	+25 12 31	61.47	0.09	2, 3, 6, 9, 11	...	Sh2−88B
G70.29+1.60	19598+3324	20 01 45.6	+33 32 44	70.29	1.60	2, 3, 4, 5, 6, 7, 12	CH	K 3−50 A
G77.96−0.01........	20277+3851	20 29 36.7	+39 01 22	77.96	−0.01	2, 3, 12	IR	...

[a] Right ascension and declination of the peak radio emission taken from the literature (equinox J2000). Units of right ascension are hours, minutes, and seconds, and units of declination are degrees, arcminutes, and arcseconds.

[b] Galactic coordinates.

[c] References for the position of the field of view.

[d] Radio morphological type from Wood & Churchwell (1989) Walsh et al. (1997), and Kurtz et al. (1994), depending on the source. (UN) Unresolved/spherical, (CO) cometary, (CH) core-halo, (SH) shell, (IR) irregular/multipeaked.

[e] Several compact radio continuum sources are included in the field of view of our near-IR images.

[f] This source has two components. Both components are included in the field of our near-IR images. Component A classified as spherical, and component B as irregular.

References.—(1) Walsh et al. 1997; (2) Bronfman et al. 1996; (3) Lockman 1989; (4) Roelfsema et al. 1988; (5) Afflerbach et al. 1996; (6) Braz & Epchtein 1983; (7) Blitz et al. 1982; (8) Walsh et al. 1998; (9) Solomon et al. 1987; (10) Churchwell et al. 1978; (11) Wood & Churchwell 1989; (12) Kurtz et al. 1994.

formation. Basic stellar properties derived from the resulting color information are also discussed. The stellar population inferred from the near-IR photometry, and in particular, the population of possible ionizing stars is compared with existing predictions based on radio, millimeter, and mid-IR data.

2. OBSERVATIONS AND DATA REDUCTION

2.1. *ALFA Observations*

The observations using the AO system ALFA (Hippler et al. 1998) on the 3.5 m telescope at the German-Spanish astronomical center on Calar Alto (Spain), were part of the ALFA science verification program. This program was carried out from fall 1999 to fall 2000. The data for the catalog presented here were taken in the month of September in both years. Individual dates are given in Table 2. The science verification program ensured that the K-band seeing was always better than 1″, partly reaching values as good as 0″.3.

Omega-Cass (Lenzen et al. 1998) served as the infrared camera. The camera pixel scale was 0″.04 for G011.11−00.40

and G77.96−0.01, and 0″08 for the rest of the targets. These scales result in a field of view (FOV) of 40″ × 40″ and 80″ × 80″, respectively.

The layout of the observations was generally as follows. The AO system was locked onto the AO guide star and a first frame was taken. Then, the telescope was moved to an offset position of about 5″–10″ with respect to the original position. The AO guide star was recentered on the wavefront sensor using the field-selecting mirror (FSM) of the AO system. The AO loop was relocked and another image taken with the same total integration time. This process was repeated for a total of five dither positions to provide for a "moving sky." An overall integration time of 10 minutes was achieved in each of the three filters (J, H, and K').

2.2. *ADONIS Observations*

The ADONIS (Beuzit et al. 1994) observations were carried out in 2000 March. The general strategy was the same as for the ALFA observations. However, for the dither pattern, it was not necessary to move the telescope, since for the ADONIS

TABLE 2

Observations and Data Quality

Object (1)	Date Observed (2)	Instrument/Telescope[a] (3)	Photometric Calibrator (4)	Bands Available (5)	SR/FWHM[b] (Guide Star) (6)	SR/FWHM (Target) (7)
G309.92+0.48	2000 Mar 14	ADONIS/3.6 LS	1719581−355732	J, H, K	.../...[c]	0.03/0″.24
G351.16+0.70	2000 Mar 15	ADONIS/3.6 LS	1719581−355732	J, H, K	.../...[c]	0.14/0″.13
G5.89−0.39..........	2000 Sep 8	ALFA/3.5 CA	1800310−240409	J, H, K'	0.04/0″.44	0.03/0″.55
G11.11−0.40........	1999 Sep 22	ALFA/3.5 CA	AS 31−0	J, H, K'	0.21/0″.16	0.02/0″.39
G18.15−0.28........	2000 Sep 9	ALFA/3.5 CA	FS 117	J, H, K'	0.05/0″.48	0.01/0″.53
G61.48+0.09	2000 Sep 16	ALFA/3.5 CA	AS 34−0	J, H, K'	0.10/0″.5	0.03/0″.57
G70.29+1.60	2000 Sep 10	ALFA/3.5 CA	AS 35	J, H, K'	0.20/0″.22	0.14/0″.22
G77.96−0.01........	1999 Sep 22	ALFA/3.5 CA	AS 31−0	J, H, K'	0.06/0″.31	0.02/0″.37

[a] "3.6 LS" refers to the ESO 3.6 m telescope at La Silla, Chile. "3.5 CA" refers to the 3.5 m telescope at Calar Alto, Spain.

[b] Strehl ratio (SR) and full width at half-maximum (FWHM) of the PSF given at the corresponding K, or K' band.

[c] The AO guide star is not within the FOV of the IR image.

system, the FSM moves the field of view of the IR camera, instead of the wavefront sensor. The SHARP camera (Hofmann et al. 1995) was used at a pixel scale of $0\farcs1$. The images were taken in the J, H, and K bands, with a total integration time of 10 minutes per filter.

2.3. Data Reduction

The data were sky-subtracted, flat-fielded, and bad pixel–corrected following the standard near-IR reduction procedures. Dome flat-fields were taken with three different levels of illumination, always using the same integration time. In this way, the response of each individual pixel can be fitted against the median response of the detector, resulting in a good representation of small- and large-scale variations of pixel responses. Bad pixels were identified when the individual response was differing from 1.0 by more than a factor of 1.5.

A sky image was constructed for each object by median combination of several dithered frames after being corrected from flat-field. Each object frame was sky-subtracted, shifted, and averaged to produce a final mosaic. For locations where a pixel was flagged as "bad" in one (or more) of the overlapping frames, only the values from the corresponding "good" frames were taken into account. The remaining bad pixels—where no overlapping good frame could be found at all—were corrected by interpolating between neighboring pixels.

2.4. Data Quality

Table 2 shows the quality of the data in terms of resolution and Strehl ratio. Both numbers are given for the actual targets and for the AO guide star (where available). The comparison illustrates the general property of (classical) AO observation of suffering from anisoplanatism, i.e., the image quality varies across the field and it is generally worse on the targets than on the guide stars. Our best-quality target is G351.16+0.70, with a resolution of $0\farcs13$ and a Strehl ratio of 0.14 (on-source).

The FWHM was measured on unresolved sources only. When the target region does not contain such a source, the nearest available unresolved star was used. The number given corresponds to the average diameter of the PSF at half the maximum intensity measured along profiles extracted at 10 different angles.

Determining the Strehl number is slightly more complicated, since it requires the knowledge of the total flux of the unresolved source. Once the total flux is determined, a model PSF is created from the telescope properties (diameters of primary and secondary mirror, width of the spiders). The Strehl ratio is the ratio between the peak intensities of the measured and the modeled PSFs. For all images taken with the ALFA system at a sampling of $0\farcs08$ per pixel, the Strehl estimates should be seen as a lower limit owing to the possibility of placing the PSF peak in between two pixels, which slightly reduces the peak flux. Generally, the Strehl numbers should be seen as estimates only because of the difficulty of determining total stellar flux levels in crowded regions.

2.5. Photometry

Rough photometric zero points were obtained by observing standard stars immediately before and after each UC H ɪɪ region. For some targets, no separate standard stars were observed. In these cases, a point source inside the images was identified from the 2MASS[2] All-Sky Catalog of Point Sources (Cutri et al. 2003) and used for the flux calibration. The names are also listed in column (4) of Table 2.

Magnitudes were calculated using PSF-fitting photometry (DAOPHOT in IRAF[3]). The fitting radius was set to the FWHM of the PSF. The PSF was best fitted with a Gaussian core and Lorentzian wings. A quadratic variable PSF across the field of view was used to account for the anisoplanatism of the AO images. When the number of PSF stars available in the field of view was less than 9 (e.g., G309.92+0.48), a linear variation of the PSF was used. In addition, aperture photometry was performed on isolated bright sources covering each field. The aperture was chosen to be large enough to include the full PSF flux. The mean difference between the magnitudes obtained with the aperture photometry and the magnitudes resulting from PSF fitting photometry in the isolated stars was utilized to calculate an aperture correction for each image. The aperture correction was subtracted from the PSF-fitting magnitudes, to determine the final software magnitudes. Errors in these magnitudes were calculated from the maximum between the error given by the PSF-fitting algorithm and the standard deviation of the aperture correction. In a further step, software magnitudes were transformed into 2MASS magnitudes to make the data set uniform. Stars in common in our images and in the 2MASS All-Sky Catalog of Point Sources were used to determine the photometric transformation. Table 3 shows the final J, H, and K_s magnitudes in the 2MASS system for some selected stars in each UC H ɪɪ region. The final errors, shown in Table 3, are the result of propagating the errors in the software magnitudes and the errors from the linear fit used in the color transformation. Limiting magnitudes in the range between 18.5 and 19.5 mag at J, 15.8 and 17.9 mag at H, and 15.4 and 16.8 mag at K_s were achieved.

2.6. Astrometry

Astrometry was performed by matching the positions of stars in common in our images and in the 2MASS survey images. The astrometric accuracy in our images is the result of propagating the error from the fit to obtain the plate solution, and the absolute astrometric accuracy of the 2MASS catalog. The first term ranges from $0\farcs03$ to $0\farcs3$ depending on the number of stars that were available to perform the fit (never fewer than 4). The second term is $0\farcs07$–$0\farcs08$ following the explanatory supplement of the 2MASS survey. Hence, our astrometric accuracy ranges between $0\farcs08$ and $0\farcs3$. Positions of selected stars are given in columns (3) and (4) of Table 3.

3. PHYSICAL PARAMETERS

3.1. Distances

Table 4 shows the kinematical distances to our sources. The radial velocities were obtained from the literature. The velocity tracers used were CO, CS, CH_3OH, and H_2O masers, and H ɪ radio recombination lines. The Galactic rotation curve given by Wouterloot & Brand (1989) was applied $[\theta(R) = \theta_\odot(R_\odot)^{0.0362}]$. The values $R_\odot = 8.5$ kpc and $\theta_\odot = 220$ km s^{-1} were used for

TABLE 3
PHOTOMETRY

Source (1)	ID (2)	α[a] (3)	δ[a] (4)	m_J[b] (mag) (5)	m_H[b] (mag) (6)	m_{K_s}[b] (mag) (7)
G309.92+0.48	3	13 50 42.97	−61 34 56.2	9.6 ± 0.1	9.1 ± 0.1	9.0 ± 0.2
	4	13 50 42.76	−61 34 58.4	12.9 ± 0.1	12.3 ± 0.1	12.0 ± 0.2
	12	13 50 42.36	−61 35 08.0	14.5 ± 0.1	12.2 ± 0.1	11.2 ± 0.2
	13	13 50 42.07	−61 35 09.9	15.8 ± 0.1	13.7 ± 0.1	12.8 ± 0.2
	14	13 50 41.84	−61 35 10.6	. . .	15.1 ± 0.2	11.3 ± 0.2
	17	13 50 40.90	−61 35 06.8	17.7 ± 0.1	13.8 ± 0.1	11.3 ± 0.2
	39	13 50 41.78	−61 35 11.5	18.7 ± 0.2	13.6 ± 0.2	10.2 ± 0.2
G351.16+0.70	20	17 19 58.16	−35 57 32.1	11.39 ± 0.05	11.2 ± 0.2	11.1 ± 0.3
	24	17 19 58.10	−35 57 44.8	15.45 ± 0.05	14.7 ± 0.2	14.2 ± 0.3
	25	17 19 58.50	−35 57 48.6	16.04 ± 0.04	15.5 ± 0.2	14.5 ± 0.3
	27	17 19 57.67	−35 57 41.7	13.99 ± 0.06	12.5 ± 0.2	11.8 ± 0.3
	29	17 19 57.85	−35 57 50.3	14.64 ± 0.08	12.7 ± 0.2	10.7 ± 0.4
	33	17 19 57.22	−35 57 26.4	. . .	15.8 ± 0.4	13.4 ± 0.5
	34	17 19 57.31	−35 57 23.0	14.23 ± 0.05	13.3 ± 0.2	12.9 ± 0.3
	36	17 19 57.19	−35 57 20.7	. . .	15.3 ± 0.4	13.4 ± 0.3
	45	17 19 57.07	−35 57 23.8	18.0 ± 0.2	12.7 ± 0.4	10.0 ± 0.5
	46	17 19 56.85	−35 57 27.3	15.9 ± 0.1	13.1 ± 0.3	11.4 ± 0.4
G5.89−0.39	1	18 00 31.01	−24 04 08.9	11.95 ± 0.06	10.8 ± 0.2	10.4 ± 0.1
	3	18 00 30.90	−24 04 02.5	17.27 ± 0.07	15.5 ± 0.2	14.3 ± 0.1
	4	18 00 30.90	−24 03 58.8	. . .	17.2 ± 0.2	15.4 ± 0.1
	5	18 00 30.87	−24 04 04.1	16.39 ± 0.08	14.0 ± 0.2	13.0 ± 0.1
	8	18 00 30.81	−24 04 00.8	. . .	16.9 ± 0.2	15.0 ± 0.1
	12	18 00 30.59	−24 04 02.0	15.99 ± 0.06	15.2 ± 0.2	14.8 ± 0.1
	14	18 00 30.44	−24 04 00.4	. . .	16.2 ± 0.2	13.3 ± 0.2
	16	18 00 30.69	−24 03 56.0	. . .	17.1 ± 0.3	12.1 ± 0.3
	17	18 00 30.46	−24 03 57.5	. . .	16.0 ± 0.2	13.6 ± 0.2
	20	18 00 30.31	−24 04 00.2	18.3 ± 0.1	15.2 ± 0.2	13.0 ± 0.2
	24	18 00 31.28	−24 03 59.9	18.4 ± 0.1	17.1 ± 0.2	15.3 ± 0.1
	25	18 00 31.36	−24 04 08.7	18.3 ± 0.1	16.1 ± 0.2	14.8 ± 0.1
	26	18 00 31.50	−24 04 09.9	18.3 ± 0.1	16.6 ± 0.2	15.6 ± 0.1
	70	18 00 29.91	−24 04 06.3	17.07 ± 0.08	14.3 ± 0.2	12.9 ± 0.1
	76	18 00 29.31	−24 03 57.1	10.85 ± 0.06	10.5 ± 0.2	10.2 ± 0.1
	81	18 00 32.35	−24 04 27.8	16.9 ± 0.1	12.2 ± 0.2	9.8 ± 0.2
	82	18 00 32.32	−24 04 26.2	16.08 ± 0.08	13.1 ± 0.2	11.8 ± 0.1
	83	18 00 32.14	−24 04 27.3	18.6 ± 0.2	13.5 ± 0.2	11.7 ± 0.1
	86	18 00 32.33	−24 04 09.5	18.4 ± 0.1	16.2 ± 0.2	13.9 ± 0.2
	120	18 00 31.65	−24 04 14.9	14.40 ± 0.07	12.1 ± 0.2	11.0 ± 0.1
G11.11−0.40	2	18 11 32.35	−19 30 52.8	13.3 ± 0.2	10.7 ± 0.1	9.6 ± 0.2
	3	18 11 32.20	−19 30 49.7	15.2 ± 0.1	14.1 ± 0.1	13.8 ± 0.1
	4	18 11 31.54	−19 30 41.4	17.4 ± 0.2	14.9 ± 0.1	14.1 ± 0.2
	8	18 11 32.07	−19 30 42.7	. . .	17.3 ± 0.2	14.6 ± 0.4
	9	18 11 31.98	−19 30 40.9	. . .	16.3 ± 0.2	14.6 ± 0.3
	10	18 11 32.71	−19 30 44.8	16.4 ± 0.2	14.2 ± 0.1	13.1 ± 0.2
	11	18 11 32.65	−19 30 43.7	14.1 ± 0.1	13.4 ± 0.1	13.2 ± 0.1
	12	18 11 31.85	−19 30 38.7	18.6 ± 0.4	14.1 ± 0.2	12.3 ± 0.3
	15	18 11 32.18	−19 30 38.3	16.5 ± 0.1	15.5 ± 0.1	15.5 ± 0.1
	22	18 11 31.40	−19 30 28.5	. . .	15.8 ± 0.2	13.2 ± 0.5
	33	18 11 33.14	−19 30 31.3	9.4 ± 0.1	9.05 ± 0.09	9.0 ± 0.1
G18.15−0.28	31	18 25 01.96	−13 16 13.4	14.22 ± 0.08	13.0 ± 0.1	12.44 ± 0.09
	49	18 25 01.82	−13 16 10.5	16.08 ± 0.09	14.3 ± 0.1	13.2 ± 0.1
	59	18 25 00.93	−13 16 06.8	17.0 ± 0.1	14.9 ± 0.1	13.7 ± 0.1
	63	18 25 01.21	−13 16 03.1	14.52 ± 0.08	13.2 ± 0.1	12.71 ± 0.09
	79	18 25 00.14	−13 15 56.1	16.2 ± 0.1	14.0 ± 0.2	13.2 ± 0.1
	85	18 25 00.40	−13 15 54.9	11.90 ± 0.07	11.1 ± 0.1	10.80 ± 0.09
	92	18 25 02.24	−13 15 54.3	17.4 ± 0.1	15.2 ± 0.2	14.3 ± 0.1
	113	18 25 01.15	−13 15 48.9	9.35 ± 0.06	8.8 ± 0.1	8.71 ± 0.09
	119	18 25 01.71	−13 15 46.4	15.06 ± 0.09	13.5 ± 0.1	12.8 ± 0.1
	120	18 25 00.58	−13 15 45.5	17.5 ± 0.1	15.4 ± 0.2	14.2 ± 0.1
	121	18 25 01.12	−13 15 44.4	15.0 ± 0.1	13.1 ± 0.1	11.9 ± 0.1
	143	18 25 01.65	−13 15 41.4	12.23 ± 0.08	10.8 ± 0.1	10.09 ± 0.09
	144	18 25 01.12	−13 15 40.1	16.8 ± 0.1	13.5 ± 0.2	11.6 ± 0.1
	147	18 25 00.50	−13 15 37.9	15.47 ± 0.07	14.5 ± 0.1	13.85 ± 0.09
	153	18 25 01.99	−13 15 32.9	12.69 ± 0.06	12.1 ± 0.1	11.84 ± 0.09

TABLE 3—*Continued*

Source (1)	ID (2)	α^a (3)	δ^a (4)	$m_J{}^b$ (mag) (5)	$m_H{}^b$ (mag) (6)	$m_{K_s}{}^b$ (mag) (7)
	155	18 24 58.38	−13 15 29.7	14.6 ± 0.1	12.4 ± 0.2	11.7 ± 0.1
	159	18 24 59.09	−13 15 27.5	17.7 ± 0.1	14.8 ± 0.2	13.5 ± 0.1
	169	18 25 02.33	−13 15 19.6	12.48 ± 0.08	11.3 ± 0.1	10.95 ± 0.09
	173	18 25 01.43	−13 15 17.9	15.2 ± 0.1	13.3 ± 0.1	12.4 ± 0.1
	175	18 25 00.17	−13 15 14.7	12.98 ± 0.08	11.7 ± 0.1	11.38 ± 0.09
G61.48+0.09	13	19 46 49.13	25 12 07.2	15.7 ± 0.1	13.54 ± 0.08	12.2 ± 0.1
	19	19 46 46.92	25 12 13.4	10.3 ± 0.1	9.65 ± 0.08	9.34 ± 0.09
	50	19 46 47.83	25 12 30.2	16.6 ± 0.1	14.31 ± 0.09	12.7 ± 0.1
	61	19 46 47.12	25 12 34.1	14.7 ± 0.1	13.01 ± 0.08	12.1 ± 0.1
	82	19 46 47.60	25 12 45.6	16.1 ± 0.1	12.2 ± 0.1	9.4 ± 0.2
	83	19 46 47.32	25 12 45.6	13.4 ± 0.1	11.84 ± 0.08	10.8 ± 0.1
	84	19 46 47.05	25 12 45.8	14.4 ± 0.1	13.17 ± 0.08	12.3 ± 0.1
	111	19 46 47.29	25 12 59.8	15.9 ± 0.1	13.52 ± 0.09	12.0 ± 0.1
	112	19 46 49.05	25 13 00.7	11.9 ± 0.1	11.35 ± 0.08	11.07 ± 0.09
	116	19 46 48.35	25 13 02.9	18.2 ± 0.1	14.83 ± 0.09	12.7 ± 0.1
G70.29+1.60	11	20 01 46.93	33 32 52.2	15.82 ± 0.06	14.82 ± 0.06	14.5 ± 0.1
	29	20 01 46.32	33 32 35.1	13.64 ± 0.06	12.86 ± 0.06	12.7 ± 0.1
	47	20 01 45.98	33 32 37.6	19.4 ± 0.1	17.11 ± 0.07	15.6 ± 0.1
	52	20 01 45.61	33 32 32.7	19.09 ± 0.09	16.17 ± 0.08	14.4 ± 0.1
	67	20 01 45.87	33 32 43.7	16.66 ± 0.06	15.22 ± 0.07	13.7 ± 0.1
	68	20 01 45.69	33 32 43.4	15.96 ± 0.09	12.46 ± 0.09	9.1 ± 0.2
	76	20 01 44.95	33 32 38.4	9.73 ± 0.06	9.14 ± 0.06	9.1 ± 0.1
	126	20 01 42.30	33 32 37.7	12.86 ± 0.06	12.05 ± 0.06	11.9 ± 0.1
	137	20 01 42.48	33 32 20.8	13.75 ± 0.06	13.33 ± 0.06	13.3 ± 0.1
	181	20 01 45.75	33 32 24.7	18.25 ± 0.08	15.28 ± 0.08	13.8 ± 0.1
	198	20 01 44.49	33 32 03.2	11.22 ± 0.06	10.58 ± 0.06	10.5 ± 0.1
G77.96−0.01........	4	20 29 37.29	39 01 18.5	17.7 ± 0.1	16.29 ± 0.05	14.41 ± 0.09
	7	20 29 36.95	39 01 22.5	12.07 ± 0.08	10.84 ± 0.05	10.21 ± 0.06
	9	20 29 36.78	39 01 22.6	15.5 ± 0.2	13.99 ± 0.04	12.94 ± 0.05
	10	20 29 36.90	39 01 26.0	...	15.83 ± 0.06	14.33 ± 0.08
	11	20 29 36.66	39 01 22.0	...	15.38 ± 0.06	12.27 ± 0.05
	16	20 29 36.54	39 01 04.4	17.09 ± 0.09	14.28 ± 0.07	12.94 ± 0.08
	19	20 29 35.54	39 00 54.5	14.66 ± 0.09	12.50 ± 0.06	10.84 ± 0.09
	23	20 29 35.97	39 01 12.7	9.16 ± 0.08	8.46 ± 0.05	8.17 ± 0.06
	30	20 29 35.09	39 01 10.5	10.88 ± 0.08	10.74 ± 0.05	10.59 ± 0.06
	45	20 29 37.38	39 01 13.8	12.08 ± 0.08	11.01 ± 0.05	10.38 ± 0.06

[a] Right ascension and declination in equinox J2000. Units of right ascension are hours, minutes, and seconds, and units of declination are degrees, arcminutes, and arcseconds.
[b] Magnitudes in the 2MASS photometric system.

the distance from the Sun to the Galactic center and the tangential solar velocity, respectively.

The calculated values for the distance to the Sun ($D_\odot$) and the distance to the Galactic center ($D_{\rm gal}$) are listed in Table 4. In some cases, the distances quoted in the literature are slightly different from the values shown here. This can be due, for instance, to the use of a different Galactic rotation curve. For the sources within the solar circle, we chose always the solution of the near distance, since the solution of the far distance would lead to unrealistic (overluminous) spectral types for most of the stars in the field of view.

For all sources but G11.11−0.40 and G61.48+0.09, an average of the values given in Table 4 was adopted as the distance to the region, since all velocity tracers are in reasonable agreement with each other. We used the standard deviation of the average as the error in the distance. For G11.11−0.40, our calculation of the kinematical distance yields only one value, 17 kpc. The adoption of this distance would imply unrealistically bright magnitudes for most of the stars in the field of view of G11.11−0.40. Hence, we use the distance of 5.2 kpc from Kurtz et al. (1994). For G61.48+0.09, we found rather discrepant velocities depending on the tracers. We adopt a

distance of 2.7 kpc, which is close to the most accepted values (see Deharveng et al. 2000).

3.2. *Ionizing Sources*

3.2.1. *Near-IR Photometry*

The definition of a near-IR source as a possible ionizing source of the UC H II region is somewhat dependent on the region. This is in part due to the fact that some H II regions, defined as *ultracompact* in a high-resolution configuration of the VLA, are in fact extended over a few parsecs (e.g., Kurtz et al. 1999; Kim & Koo 2001) at lower spatial resolution configurations, which are more sensitive to larger spatial scales. Uncertainties in the distance and in the spectral type derived from our photometry also affect the determination of sources possibly ionizing the UC H II region. We consider a source to be a candidate for ionizing an H II region when it is located within a projected distance of 0.5 pc from the radio-emission peak. This value corresponds to the upper limit for the size of compact H II regions. Another condition is that the spectral type inferred from our photometry should be earlier than B5 V. However, these requirements are not sufficient. Potential

TABLE 4
DISTANCE ESTIMATES

Object (1)	V_{LSR} (km s^{-1}) (2)	Tracer (3)	D_{gal} (kpc)[a] (4)	$D_{\odot}$ (kpc)[a] (5)	σ (6)	Reference[b] (7)
G309.92+0.48[c]	−58.4	CS	6.5	5.5	...	2
	−60	CH$_3$OH	6.5	5.5	...	1
	−74	H$_2$O	6.5	5.5	...	6
	−59.9	CH$_3$OH	6.5	5.5	...	8
G351.16+0.70	−5	CH$_3$OH	7.3	1.2	(15.6)	1
	−3.4	H85α	7.7	0.8	(16.0)	3
	−6	H$_2$O	7.2	1.3	(15.5)	6
	−6.3	CH$_3$OH	7.1	1.4	(15.4)	8
G5.89−0.39.........	9.3	CS	5.9	2.6	(14.3)	2
	10.1	H100α	5.8	2.7	(14.2)	3
	5.0	H76α	6.9	1.6	(15.3)	5
	14	H$_2$O	5.1	3.4	(13.5)	6
	9.6	H$_2$O	5.9	2.6	(14.3)	8
G11.11−0.40.......	−1.1	CS	8.8	...	16.9	2
	−2	CO	9.0	...	17.1	9
G18.15−0.28.......	54.9	CS	4.6	4.3	(11.9)	2
	53.9	H85α	4.6	4.3	(11.9)	3
	54	CO	4.6	4.3	(11.9)	9
	53.5	H109α	4.7	4.2	(11.9)	10
G61.48+0.09[d]	21.9	CS	7.6	2.7	(5.5)	2
	27.3	H85α	7.5	4.1	...	3
	30	H$_2$O	7.5	4.1	...	6
	22	CO	7.6	2.7	(5.5)	9
G70.29+1.60	−25.2	CS	9.7	8.4	...	2
	−24.5	H85α	9.7	8.3	...	3
	−27.5	H110α	9.8	8.4	...	4
	−19	H$_2$O	9.4	7.8	...	6
	−24.5	CO	9.7	8.3	...	7
G77.96−0.01.......	−2.9	CS	8.6	4.1	...	2
	−5.5	H85α	8.7	4.4	...	3

[a] Kinematical distances to the Galactic center (col. [4]) and to the Sun (col. [5]) calculated from the radial velocities in col. (2). For the sources within the solar circle, the solution for the far distance is shown in parentheses.
[b] References for the local standard of rest velocity (V_{LSR}) and velocity tracers.
[c] The tanget point was used, since no solution was found.
[d] The tanget point was used for H85α and H$_2$O, since not solution was found.

REFERENCES.—(1) Walsh et al. 1997; (2) Bronfman et al. 1996; (3) Lockman 1989; (4) Roelfsema et al. 1988; (5) Afflerbach et al. 1996; (6) Braz & Epchtein 1983; (7) Blitz et al. 1982; (8) Walsh et al. 1998; (9) Solomon et al. 1987; (10) Churchwell et al. 1978.

ionizing sources should appear as pointlike in our near-IR images. There should also be features in the images that link them with the radio peak, e.g., near-IR nebulosities. We discard as possible ionizing sources any bright stars whose colors and low extinction indicate their being foreground stars (see § 4.2.1). Finally, we associate a spectral type to each source in the FOV based on its location in color-color (C-C) ($J − H$ vs. $H − K_s$) and color-magnitude (C-M) (K_s vs. $H − K_s$) diagrams.

In each diagram, we plot the theoretical main sequence (MS) and the giant and supergiant branches, at the assumed distance for each UC H II region. Intrinsic stellar colors were taken from Tokunaga (2000).[4] The earliest dwarf for which intrinsic colors are available has a spectral type O6 V, and therefore, in the C-M diagrams we plot the main sequence up to this spectral type. For the giant and supergiant branches, we also plot only the spectral type ranges available in Tokunaga (2000). Ducati et al. (2001) show more recent stellar intrinsic colors, but they do not reach dwarf spectral types earlier than

B0 V. We therefore adopt the colors from Tokunaga rather than those from Ducati et al. for consistency, since the latter lack spectral types for O V stars.

Absolute visual magnitudes were taken from Aller et al. (1982). The association between M_v and the intrinsic colors was made by matching the spectral types of Aller et al. (1982) with those of Tokunaga (2000). Hence, we used the calibration of the M_v–spectral type relation given in Aller et al. (1982). Other possible calibrations of M_v as a function of the spectral type are available in Vacca et al. (1996) and Smith et al. (2002). For early-type stars (O3, O4, O5), a calibration is also available in Crowther & Dessart (1998). However, the latter three were not used in our C-C and C-M diagrams, since they only have a limited spectral type coverage compared with the calibration by Aller et al. (1982). The typical errors associated with the M_v are ∼0.5 mag (see Vacca et al. 1996), which is larger than the typical error in our photometry. Hence, our spectral type classification based on near-IR photometry is not strongly affected by the M_v–spectral type relation.

The following procedure was used to determine spectral types based on the near-IR photometry. From the location of a

[4] Available at http://www.jach.hawaii.edu/JACpublic/UKIRT/.

star in the C-C diagram with respect to the unreddened main sequence, its intrinsic color excess and extinction were estimated. In most of the cases, sources with intrinsic near-IR excess appear to the right of the reddened MS. This $H - K_s$ excess was assumed to be only due to a K_s excess, probably due to emission lines associated with photoionization and/or wind shocks, and/or continuum excess caused by accretion luminosity. Hence, we consider this excess independent of the extinction. The K_s excess was evaluated by measuring the distance along the line $J - H$ constant for the star between the point representing the star in the C-C diagram and the extincted main sequence. The extinction toward this star was then obtained by measuring the length of the reddening vector between the unreddened MS and the line $J - H$ constant for the star. Once intrinsic K_s excess and reddening were known for a given star, its K_s excess was first removed along the $H - K_s$ and K_s axes in the C-M diagram, to obtain a new point representing the star without intrinsic near-IR excess. Second, this point was projected onto the unreddened MS (and giant and supergiant branches) following a line parallel to the reddening vector. The spectral type was then read directly from the unreddened MS (and giant and supergiant branches).

This method of spectral type determination, even though it is rather qualitative, it is reasonable for the typical uncertainties associated with the distances and with our measurements. A 25% decrease in the distance, for instance, implies a shift of the MS of about 0.5 mag toward brighter magnitudes, which in turn implies a shift of ∼5 subtypes in the spectral type classification of a star. Typical errors in our measurements are slightly smaller, yielding similar uncertainties in the classification. Other sources of uncertainty are due to the M_v–spectral type relation used (∼0.5 mag, see above) and due to the assumption of a universal extinction law. The latter is difficult to estimate, but different extinction laws toward each region due to different dust properties, would yield changes on the reddening vector slope in the C-C and C-M diagrams, which would affect the spectral type determination.

3.2.2. *Radio*

In Table 5, we give the spectral type of the ionizing star derived from radio-continuum observations found in the literature, taking our distances into account. For half of regions (G5.89-0.39, G18.15-0.28, G61.48+0.09, and G70.29+1.60), the spectral type given by the authors in the references of column (5) was transformed into a Lyman continuum photon rate (N_L) using the same stellar model grids as those adopted by the original authors (normally, Panagia 1973 or Vacca et al. 1996). This number was scaled to our assumed distance (col. [2]) for each source. The scaled log (N_L) is listed in column (4). The log (N_L)–spectral type relation given in the stellar model grids from Vacca et al. (1996) and Smith et al. (2002) was used to infer our new estimate of the spectral type for the ionizing source (cols. [6] and [7], respectively). In the case of G309.92+0.48, G351.16+0.70, and G77.96−0.01, for which there are no previous estimates of the Lyman photon rate, the N_L was calculated directly from the radio flux densities given in Walsh et al. (1998), Jackson & Kraemer (1999), and Kurtz et al. (1994), respectively. Equations (1) and (3) in Kurtz et al. (1994) for optically thin H II regions were applied. For G11.11−0.40, we also used these equations to estimate the log (N_L) from the radio flux density given in Kurtz et al. (1994). In these four sources, the same log (N_L)–spectral type relations as for the rest of the UC H II regions was applied to determine the spectral type of the ionizing source. No error is given in the log (N_L) for any of the UC H II regions because the original references for the radio data do not provide any error in the N_L or in the integrated radio fluxes. An error based only on the statistical uncertainties would be negligible compared with the systematic errors implicit in the equations used to calculate the log (N_L) (e.g., distance, assumption of optically thin emission or assumption of a geometry).

3.3. *IRAS and MSX Luminosities*

In Table 5, we also list the spectral type deduced from the mid- and far-IR luminosity of the *IRAS* source associated with each UC H II region. In all sources, we first apply the standard procedure to estimate the total luminosity (L_{TOT}) based on the *IRAS* fluxes taken from the *IRAS* Point Source Catalog (PSC, version 2.0). This consists of adding the total flux in each of the *IRAS* bands using the formula given in Walsh et al. (1997) (see also Henning et al. 1990). The total flux was divided by a correction factor that accounts for the flux at longer wavelengths than the *IRAS* 100 μm band. We assumed a value of 0.61 ± 0.02 for this factor (Walsh et al. 1997). The luminosity (L_{TOT} in col. [8]) was calculated at the distances listed in column (2). This luminosity was then used to derive a spectral type (cols. [9] and [10]), assuming one single heating star. The spectral type for a given L_{TOT} was read directly off Tables 5, 6, and 7 in Vacca et al. (1996) to yield the entries of column (9). From the Smith et al. grid, the L_{TOT} was first transformed into a stellar effective temperature (T_{eff}) by using the grid of Vacca et al. (1996). Second, the T_{eff}–spectral type relation given in Smith et al. (2002) was used to derive the spectral type. One of the main drawbacks of this spectral type classification is that the *IRAS* beam is ∼2′ in size, i.e., it covers completely the field of view of our images. Hence, the assumption that only one star is contributing to the total luminosity derived from *IRAS* fluxes should be taken with extreme caution in the majority of cases. In Table 5, errors in the luminosities are also given, which result from propagating the uncertainties in the *IRAS* fluxes, in the distance, and in the luminosity correction factor.

In this work, we also make use of the *MSX* PSC (version 2.3, Egan et al. 2003), which traces relatively warm dust, with better spatial resolution than *IRAS*. The beam size of *MSX* is ∼20″, which yields a lower source confusion than *IRAS*. To characterize the *MSX* spectrum of the UC H II regions in our sample, we made a blackbody fit to the *MSX* bands at 14.65 and 21.34 μm. The reason for not including in the fit the *MSX* bands centered at 8.28 and 12.13 μm is that they are highly dominated by polycyclic aromatic hydrocarbon (PAH) emission bands as well as the silicate feature at 9.7 μm (see Peeters et al. 2002). Inspection of the *ISO* spectra of UC H II regions presented in Peeters et al. (2002) shows that a blackbody fit, even in the relatively featureless range between 14 and 21 μm, is a poor representation of the general shape of the spectral energy distribution. The luminosity associated with each *MSX* source (L_{MSX}) is listed in column (11) of Table 5. The quoted errors result from the propagation of the errors in the blackbody's temperature and scaling factor (given by the fitting routine) and the errors in the distances.

4. RESULTS

We now focus on the near-IR morphology of each UC H II region individually (§ 4.1). The stellar population is also discussed, particularly the most likely candidates for ionizing stars. The luminosity and Lyman photon rate of these near-IR stars is compared with those inferred from *IRAS* and radio

TABLE 5

PHYSICAL PARAMETERS

Object (1)	$D_\odot$[a] (kpc) (2)	Spectral Type[b] (This Work) (3)	$\log(N_L)$[c] (4)	Refs[d] (5)	Spectral Type[e] (Radio) (6)	Spectral Type[f] (Radio) (7)	L_{TOT}[g] ($10^4\ L_\odot$) (8)	Spectral Type[e] (IRAS) (9)	Spectral Type[f] (IRAS) (10)	L_{MSX}[h] ($10^4\ L_\odot$) (11)
G309.92+0.48	5.5[i]	>O6 V/O I	48.0	1	B0 V	O9 V	32 ± 2	O6.5 V	O5 V	11 ± 3
G351.16+0.70[j]	1.2 ± 0.2	O6 V	47.3	2	<B0.5 V	B0 V	4 ± 1	<B0.5 V	<B0 V	0.9 ± 0.4
G5.89−0.39..........	2.6 ± 0.6	O3 V[k]	48.6	3	O9 V	O8 V	27 ± 13	O7 V	O7 V	5 ± 3
G11.11−0.40........	5.2[i]	O6 V	47.8	4	<B0.5 V	O9 V	7.4 ± 0.8	B0 V	O9 V	1.4 ± 0.4
G18.15−0.28........	4.3 ± 0.1	O6 V	46.8	4	<B0.5 V	B0.5 V	23 ± 2	O7 V	O7 V	0.71 ± 0.04
G61.48+0.09B1....	2.7[i]	O9 I	48.4	5	O9.5 V	O8 V	17 ± 1	O8 V	O7.5 V	5 ± 1
G61.48+0.09B2....	2.7[i]	B0 V	46.5	3	<B0.5 V	B0 V	17 ± 1	O8 V	O7.5 V	5 ± 1
G70.29+1.60	8.2 ± 0.2	>O6 V/A0 I	49.2	4	O6.5 V	O5 V	200 ± 16	>O3 V	>O3 V	52 ± 15
G77.96−0.01........	4.2 ± 0.2	O8 V	46.5	4	<B0.5 V	B1 V	9.6 ± 1	O9.5 V	O8 V	4 ± 1

[a] Average distance from Table 4. The errors correspond to the standard deviation of the mean.

[b] Spectral type of the best candidate for ionizing source from our near-IR data. The symbol "<" denotes "*later than*" spectral types. The symbol ">" denotes "*earlier than*" spectral types.

[c] N_L is the number of Lyman continuum photons in units of s^{-1} at the distance of col. (2), inferred from the radio continuum data shown in the references of col. (5).

[d] References for the radio source used to determine spectral type.

[e] Spectral type using the model grid of Vacca et al. (1996). A caveat should be noted here because of the large *IRAS* beam size.

[f] Spectral type using the model grid of Smith et al. (2002). A caveat should be noted here because of the large *IRAS* beam size.

[g] Total luminosity in units of $10^4\ L_\odot$ used to determine the spectral type; L_{TOT} is calculated from the *IRAS* fluxes extracted from the *IRAS* PSC.

[h] *MSX* luminosity in units of $10^4\ L_\odot$ calculated from the integrated flux in a blackbody fit to the *MSX* fluxes at 14.65 and 21.34 μm.

[i] No statistical error is given for G309.92+0.48, since all velocity tracers yield the same distance. For G11.11-0.40 and G61.48+0.09, the most accepted distance found in the literature is adopted, hence no error is given either.

[j] Complex of compact radio-continuum sources. The radio spectral determination is from the large-scale shell structure (Jackson & Kraemer 1999).

[k] Spectral type from Feldt et al. (2003) scaled to our adopted distance.

REFERENCES.—(1) Walsh et al. 1998; (2) Jackson & Kraemer 1999; (3) Wood & Churchwell 1989; (4) Kurtz et al. 1994; (5) Deharveng et al. 2000.
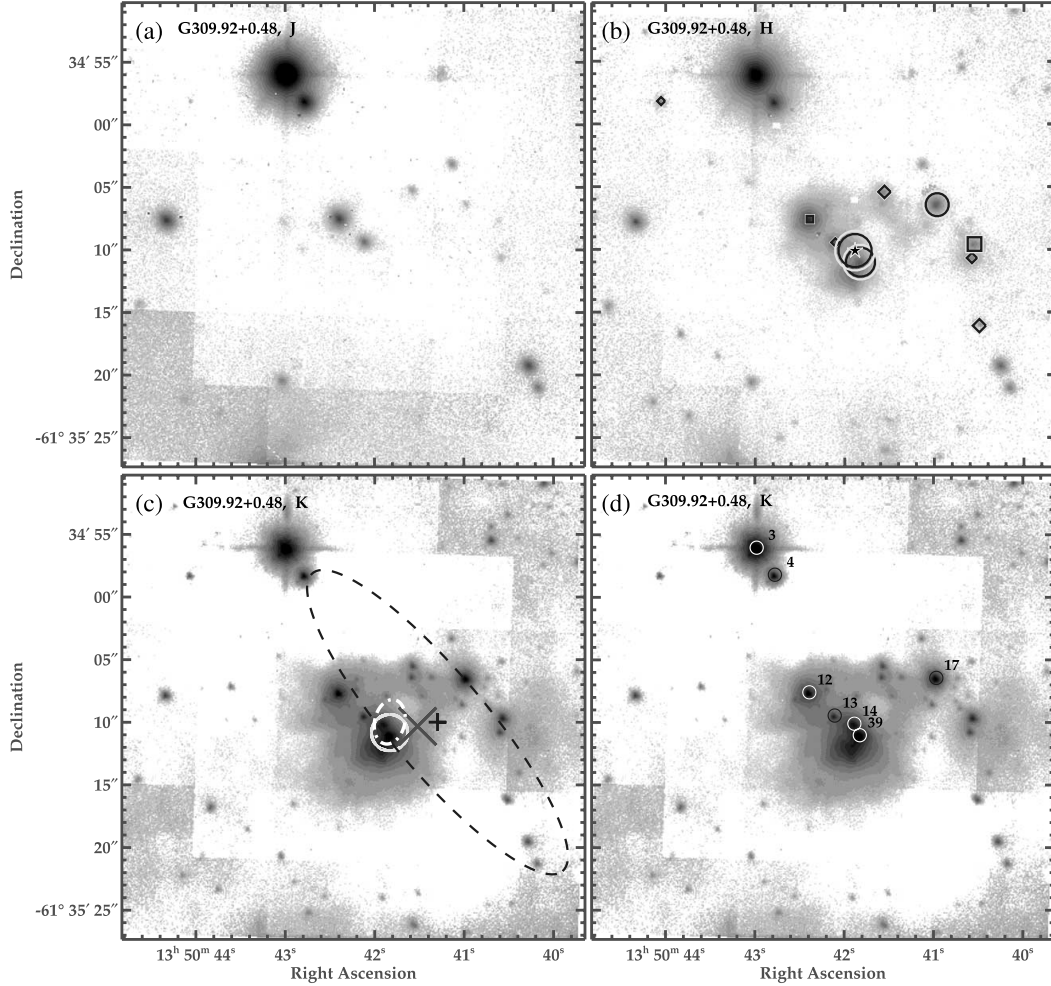
Fɪɢ. 1.—Near-IR images of G309.92+0.48. (*a*) *J*-band image. The gray scale varies from 12.0 mag arcsec^{-2} (*dark*) to 20.5 mag arcsec^{-2} (*white*). The sharp-edged gray features in the background are artifacts from the mosaics and are shown to illustrate the noise level in the images. (*b*) *H*-band image. The gray scale varies from 9.0 to 19.5 mag arcsec^{-2}. The symbols represent stars whose $J - H$ and $H - K_s$ colors are above certain cutoff values (see Fig. 2 and explanation in § 4.2.1). Stars with spectral types earlier than O3 V are represented by open circles. Spectral types in the range O9 V–O3 V are represented by open squares. B9 V–B0 V types are represented by diamonds, and A9 V–A0 V are represented by triangles (none appear in this figure). Pentagon-labeled stars (none appear in this figure) have spectral types later than A9 V. The size of the symbols is proportional to the $H - K_s$ color. Stars of any spectral type with intrinsic near-IR excess are labeled with a dark five-pointed star of fixed size. (*c*) *K*-band image. The gray scale varies from 10.0 to 20.5 mag arcsec^{-2}. The solid circle represents the radio emission at 3.6 cm from (Walsh et al. 1998). The plus symbol and the dashed ellipse represent the position and 1 σ positional error ellipse of the *IRAS* source. The *MSX* positional error ellipse (3 σ) is plotted as a thick gray dot-dashed ellipse. The large thick cross indicates the position of the CS core from Bronfman et al. (1996). The cross size indicates the pointing error of the CS peak. (*d*) Some of the sources selected to produce the color-color and color-magnitude diagrams of Figure 2 are labeled on the *K*-band image. In these and the following images shown in this paper, north is up and east is to the left. [*See the electronic edition of the Supplement for a color version of this figure.*]

continuum data. More emphasis is given to the description of the regions whose near-IR subarcsecond morphology has not been deeply studied before (G309.92+0.48, G351.16+0.70). Sources for which detailed adaptive optics near-IR data are already published are discussed less deeply (e.g., G5.89−0.39, Feldt et al. 1999; G11.11−0.40, Henning et al. 2001). In § 4.2, we analyze the general properties of the sample.

4.1. *Discussion on Individual Regions*

Even though in Table 5 the stellar model grids by Vacca et al. (1996) and Smith et al. (2002) have been included for comparison, in the following discussion on each individual object, only the grid by Smith et al. (2002) is considered to determine spectral types from radio and *IRAS* data, since it is based in more realistic models than the grid by Vacca et al. (1996). In § 4.2.3, we discuss in more detail the advantages of one grid with respect to the other.

4.1.1. *G309.92+0.48*

This region was cataloged as an UC H ɪɪ region according to its *IRAS* colors (Bronfman et al. 1996). It was classified as unresolved by Walsh et al. (1998) based on their radio-continuum observations. G309.92+0.48 is known to be associated with H$_2$O, OH, and methanol maser emission (Braz & Epchtein 1983; Walsh et al. 1999).

Low-resolution NIR photometry of G309.92+0.48 was obtained by Epchtein et al. (1981) and Epchtein & Lepine (1981). More recently, the region was imaged in the near-IR at the seeing limit by Walsh et al. (1999) and at subarcsecond resolution by Henning et al. (2002). Figure 1 shows our new near-IR images of this source taken with ADONIS at a resolution of ∼0″.2. An extended diffuse near-IR nebula around the radio peak is seen prominently in the *K*-band image. The nebular core, which is located inside the 3.5 cm emitting region detected by Walsh et al. (1998) (Fig. 1*c*, *white solid-line*
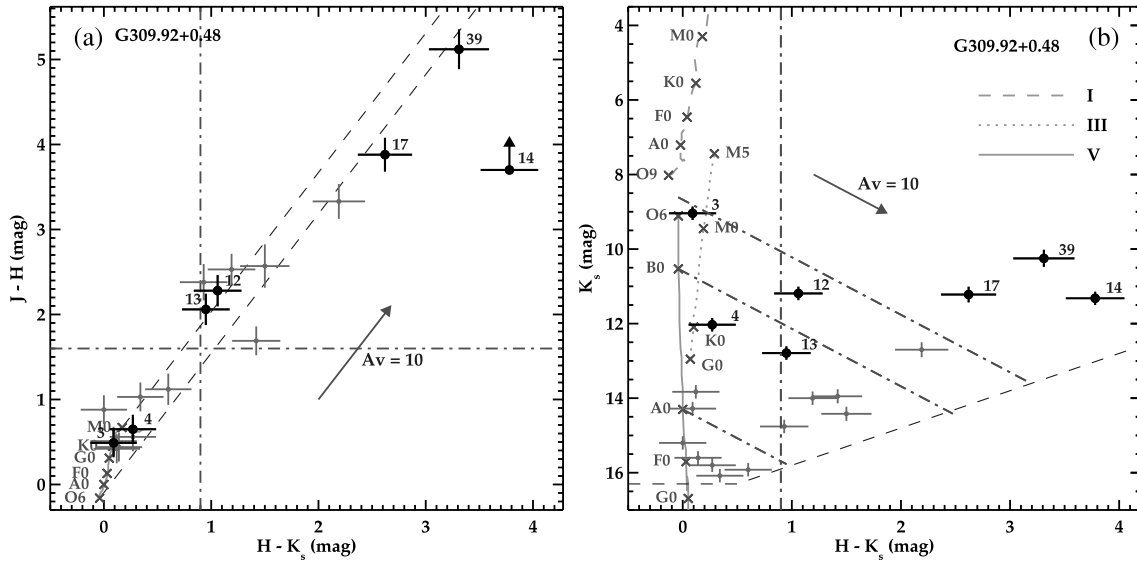
Fig. 2.—(*a*) Color-color diagram of G309.92+0.48. The gray solid line at the bottom left of the diagram represents the main sequence, where some spectral types are marked with crosses. The dashed lines show the reddened main sequence. The arrow represents a visual extinction of 10 mag. The colors of most of the sources in our images are represented by gray error bars. The colors of some selected sources (listed in Table 3 and labeled in Fig. 1) are represented by black circles with error bars. Some of these sources (12, 13, 14, 17 and 39) have been selected because they are bright in the K band, they are located near the radio peak and have considerable near-IR excess, which makes them the best candidates for ionizing sources of the UC H II region. The remaining sources (3 and 4) are bright in the three bands. They are normally bright nearby stars with hardly any extinction, and therefore, they should appear at the bottom left of the C-C diagram. Hence, they were selected to check for consistency in the photometry. These selection criteria for labeling are followed in all the remaining UC H II s shown in this paper. The arrow for source 14 indicates that it was not detected in the J filter. The vertical and horizontal dot-dashed lines represent the $H - K_s$ and $J - H$ color cutoffs between foreground stars and stars likely belonging to the UC H II region (see discussion in § 4.2.1). (*b*) Color-magnitude diagram of G309.92+0.48 at a distance of 5.5 kpc. The unreddened main sequence is represented by the gray solid line. The dotted line is the giant branch and the gray dashed line represents the supergiant branch. Spectral types are indicated by crosses along each branch. A reddening vector of 10 visual magnitudes is represented by a gray arrow. The dark dashed line is our detection limit. The colors of several sources measured in our near-IR images are represented with the same symbols as in (*a*). The vertical dot-dashed line represents the same $H - K_s$ color cutoff as in (*a*). Dot-dashed lines parallel to the extinction arrow separate different spectral types. The upper of these lines corresponds to an spectral type O3 V, whose M_v is 0.5 mag brighter than that of an O6 V star (Vacca et al. 1996) and we assume to have the same intrinsic colors as an O6 V star. [*See the electronic edition of the Supplement for a color version of this figure.*]

circle), is predominantly extended toward the southeast. Our images show that the center of the 3.6 cm emission coincides with the position of source 39 (see Fig. 1) within the errors. The astrometric accuracy of our images is 0″1, while Walsh et al. (1998) quote an accuracy of 0″05 in the peak position of the 3.5 cm emission. In the K-band image shown by Walsh et al. (1999), the radio peak appears slightly displaced ($\sim 1''$) toward the south of the apparent position of source 39. We also note that the magnitudes listed in Table 1 of Walsh et al. are systematically shifted by ~ -3 mag with respect to our values for common unresolved stars. Such an increase in brightness would shift most of the stars in the C-M diagram to a zone where they would appear overluminous (at the assumed distance). We discard the possibility of variability in the sources, since the magnitude difference appears to be roughly the same in all sources. We therefore adopt our own values in the following discussion.

Figure 2 shows the color-color and color-magnitude diagram of selected stars within the field of view of our near-IR images. We have labeled with numbers the some of the brightest stars in the K band. In particular, we have labeled those sources which are located near the UC H II region, and which have considerable near-IR excess, since they are the best candidates for ionizing sources of the UC H II region. Figure 2*a* indicates that two of the most obscured sources (source 39 with $A_v \sim 60$ mag, and source 14 with $A_v > 50$ mag) are located near the peak of the 3.5 cm emission. Source 39 lies within the extincted main sequence, while source 14 appears to show some IR excess. Source 17, which is located at 8″ (i.e., 0.2 pc at the adopted

distance of 5.5 kpc) northeast of the UC H II region, is also highly extincted ($A_v \sim 45$ mag). The extinction appears to be lower toward the northwest of the UC H II region, since sources 12 and 13 have visual extinctions of ~ 25 mag.

The C-M diagram (Fig. 2*b*) is helpful in finding out which of these sources are most likely to be responsible for the ionization of the UC H II region. The C-M diagram indicates a spectral type either earlier than O6 V or approximately K0 I for source 39. However, if source 39 is a supergiant, its spectral type would be too cold (K0 I) to ionize the H II region, although it would contribute considerably to the total luminosity of the system. For source 14, a somewhat more uncertain spectral type $\sim$O9 I or earlier than O6 V is estimated once its $H - K_s$ excess is removed from the C-M diagram, following the procedure described in § 3.2.1. Source 14 could be a supergiant and still ionize the H II region. Source 17 appears to be a reddened early O V or a late A I star, which in the latter case would be too cold to be candidate for ionizing source. The location of source 12 in the C-M diagram is consistent with an intermediate O V or K III star under moderate extinction. Source 13 can be interpreted as a late O/early B Main-Sequence star or an early K III star. Hence, if we discard the possibility that stars 12 and 13 are giants, and stars 17 and 39 are supergiants, we find up to five possible ionizing sources for the UC H II region, one of which (14) could still be a supergiant.

Once the main near-IR population has been analyzed, we now focus on the radio and *IRAS* data for G309.92+0.48. A peak flux density of 350 mJy per beam at 3.5 cm (Walsh et al.

1998), a beam size of $1\rlap{.}''3$, and a T_e of 7500 K were utilized to calculate the beam temperature, optical depth, and emission measure, which yielded $\log(N_L) = 48.0$ at a distance of 5.5 kpc. The stellar models from Smith et al. (2002) indicate a O9 V spectral type for the ionizing source capable of producing such a Lyman photon rate. Any of the possible ionizing sources listed in the previous paragraph would suffice to produce such a Lyman photon rate. A total luminosity of $(3.2 \pm 0.2) \times 10^5 L_\odot$ was inferred from the fluxes of IRAS 13471−6120 given in the *IRAS* point source catalog, which indicates an O5 V spectral type for the heating source. Source 39 alone is already more luminous than the *IRAS* source. An anisotropic dust distribution in the UC H II region or the presence of undetected (obscured) stars may account for this discrepancy between the *IRAS* luminosity and the luminosity of the observed near-IR stellar population (see the general discussion in § 4.2.4).

4.1.2. *G351.16+0.70 (NGC 6334-V)*

NGC 6334-V is a far-IR source (McBreen et al. 1979; Loughran et al. 1986) in the complex star-forming region NGC 6334. In the original low-resolution map at 69 μm by McBreen et al. (1979), NGC 6334-V appears as a point source at a resolution of $\sim 3'$. The peak of NGC 6334-V is located $30''$ toward the north of IRAS 17165−3554. Radio-interferometric studies (Simon et al. 1985; Rengarajan & Ho 1996; Walsh et al. 1998; Jackson & Kraemer 1999; Argon et al. 2000) revealed several compact (radii $< 2''$) continuum sources, which are located $25''$ toward the south/southeast of the far-IR peak. Using the VLA in C configuration, Jackson & Kraemer (1999) found that several of these compact sources are included in the southern rim of a large radio-shell of $\sim 1'$ radius. The geometrical center of the shell is offset $\sim 1'$ to the northeast of NGC 6334-V. The shell shows a clumpy morphology, which leaves the question open of whether the compact continuum sources are clumps in the shell or independent sites of star formation. Some of these compact radio sources are associated with water, OH (Braz & Epchtein 1983; Argon et al. 2000), and methanol (Walsh et al. 1998) maser emission. A large-scale bipolar molecular outflow is also seen toward this star-forming region (Phillips & Mampaso 1991).

NGC 6334-V has been extensively studied at near- and mid-IR wavelengths (Harvey & Gatley 1983; Harvey & Wilking 1984; Simon et al. 1985; Straw et al. 1989; Burton et al. 2000). Up to now, the highest spatial resolution in the near-IR ($\sim 3\rlap{.}''5$) was achieved by Straw et al. (1989) and Burton et al. (2000).

In Figure 3, we present our AO-assisted images from ADONIS in the *J*, *H*, and *K*-bands, which have a resolution ~ 25 times better than previous studies. In the field of view of our images, some of the unresolved sources from Straw et al. (1989) (labeled IRS 24, IRS 25, IRS 39) appear clearly resolved into several components. The bipolar reflection nebula studied by Harvey & Wilking (1984) and Simon et al. (1985) can be seen toward the southwest in our images. Both lobes (IRS 24 and IRS 25) are clearly separated from each other and composed of several knots. Both nebular lobes are located inside the positional error ellipse of IRAS 17165−3554.

No near-IR counterpart is detected at the position of the compact radio source detected by Argon et al. (2000) (Fig. 3c, *solid ellipse*), which is located between both lobes of the nebula. This compact source is also the radio source R-E3 detected by Rengarajan & Ho (1996) (Fig. 3c, *lower right triangle*). The 20 μm source from Harvey & Wilking (1984) (Fig. 3c, *open square*) has no near-IR counterpart either. The eastern lobe of the nebula coincides with the position of

the radio continuum source R-E2 (Rengarajan & Ho 1996; Jackson & Kraemer 1999). The irregular UC H II region detected by Walsh et al. (1998), with coordinates (J2000) $\alpha = 17^h19^m59\rlap{.}^s9$, $\delta = -35°57'40''$, is off the field of view of our images. The most interesting feature in our images is the group of $\lesssim 10$ unresolved near-IR sources at the position of the source IRS 39 (Straw et al. 1989), which is coincident with the far-IR peak, NGC 6334-V.

Our C-C diagram (Fig. 4a) indicates a reddening of 30–40 mag in the visual at the location of NGC 6334-V. Source 45 (see Fig. 3d) is obscured by an A_v of ~ 40 mag. Sources 33 and 36, located within $5''$ of 45, follow in decreasing degree of obscuration, with visual extinctions greater than 30 mag each. In the same association of unresolved IR sources, 46 appears to have a visual extinction of ~ 20 mag. The extinction near the compact region R-E3 appears to be higher, since no near-IR point source is detected. Source 29, located at $3''$ to the east of R-E2, apparently has an extinction of ~ 20 mag in the visual. However, this source is clearly extended in our *K*-band image, probably a knot in the nebula IRS 25, and hence the extinction determination is very uncertain.

The C-M diagram shown in Figure 4b yields further insights into the stellar population. Associated with the far-IR source NGC 6334-V, we identify one O6 V (45) star and three B V stars (33, 36, and 46). Note that the dereddened colors of these four point sources are also consistent with spectral types in early- to mid-M III. In principle, this possibility cannot be discarded, except for the presumed youth of NGC 6334-V. In the same association, star 34 appears to be barely extincted, indicating that this is likely a foreground star. In the immediate surroundings of the R-E3 region no near-IR point source was detected, probably due to high extinction. This is supported by the presence of an *MSX* source located at the same position as RE-3.

The large-scale shell, with a radius ~ 0.3 pc, detected by Jackson & Kraemer (1999) at 3.5 cm, has an integrated flux density of 1.2 Jy. At a distance of 1.2 kpc, a $\log(N_L) = 47.3$ is needed to ionize the shell with a $T_e = 7500$ K. If we compare this value with the predictions from the stellar models of Smith et al. (2002), the inferred spectral type for the ionizing star of the large scale shell is B0 V. If the radio peaks R-E2 and R-E3 are considered to be independent UC H II regions rather than clumps (with no stars inside) forming part of the large-scale shell, similar lower limits for the spectral types are inferred from their 3.5 cm flux (1.4–1.7 mJy; Jackson & Kraemer 1999). No near-IR pointlike counterpart is found coincident with any of the compact radio sources.

We focus our attention on the compact association of near-IR point sources resolved at the position of IRS 39. We infer a spectral type for source 45 (O6 V) that would produce more than enough Lyman photons to ionize the large-scale shell. Besides, sources 33, 36, and 46 (early B V spectral types) can also play a role in the ionization of the shell. However, the fact that this stellar association is located near the southern rim of the shell rather than near the center makes it quite unlikely that they are the main ionizing sources for the whole shell. If source 45 is contributing partially to the ionization of the southern rim of the shell, it is difficult to explain why no traces of ionized gas are seen at the position of source 45 itself. The possibility that sources 45, 33, 36, and 46 are protostars can be discarded, since they show low intrinsic *K*-band excess in our C-C diagram.

Two possible spectral types can be determined for the dust heating sources from the mid- and far-IR data available for
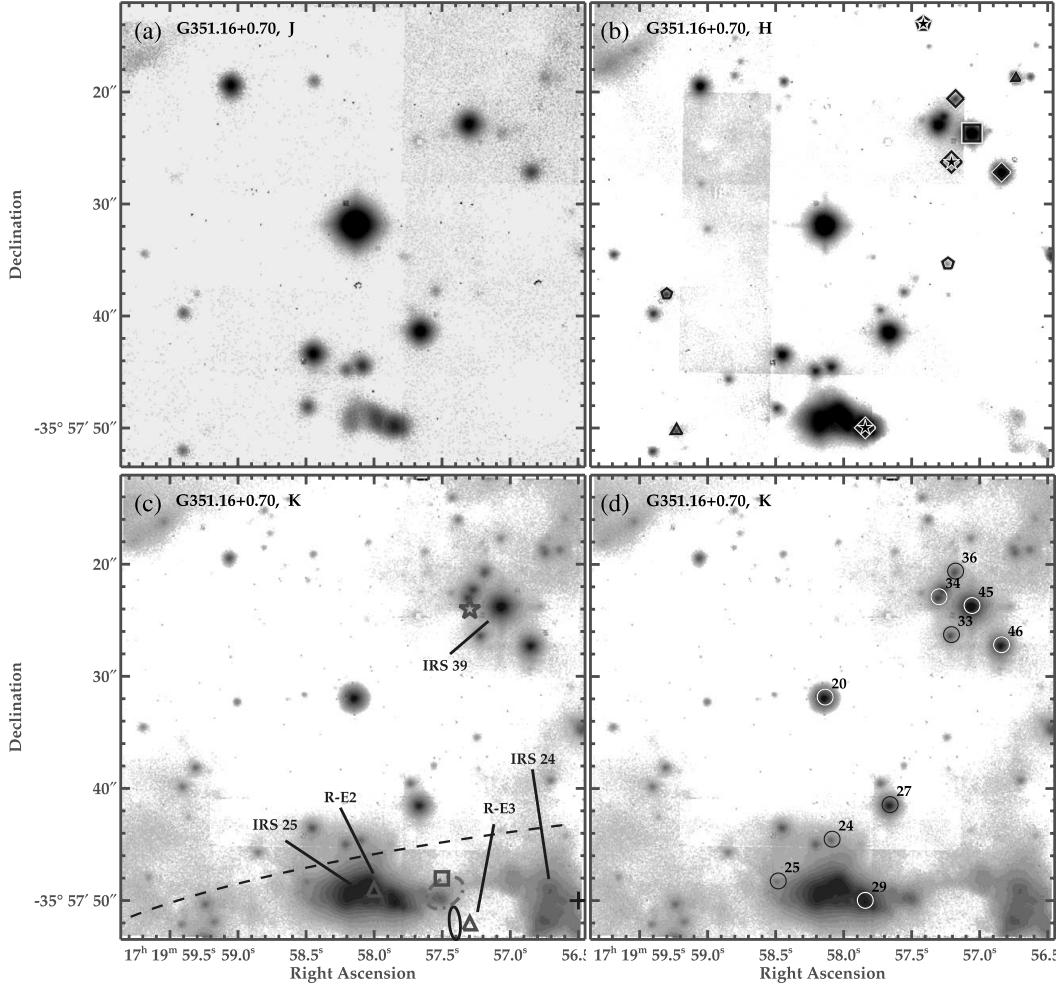
FIG. 3.—AO-assisted near-IR images of G351.16+0.70/NGC 6334-V taken with ADONIS at the 3.6 m telescope in La Silla. (*a*) *J*-band image. The gray scale varies from 14.6 mag arcsec^{-2} (*dark*) to 20.3 mag arcsec^{-2} (*white*). (*b*) *H*-band image. The gray scale varies from 13.5 to 18.4 mag arcsec^{-2}. See Fig. 1 for a key to the symbols. (*c*) *K*-band image. The gray scale varies from 9.8 to 18.9 mag arcsec^{-2}. The small solid ellipse represents the 3.5 cm continuum emission from Argon et al. (2000). The triangles indicate the location of the radio-continuum sources R-E2 and R-E3 from Rengarajan & Ho (1996) (see also Jackson & Kraemer 1999). The plus symbol and the dashed line represent the position and positional error ellipse of the *IRAS* source. The five-pointed star represents the central position of the far-IR source NGC 6334-V from McBreen et al. (1979). The open square indicates the location of the 20 μm source from Harvey & Wilking (1984). The near-IR sources IRS 24, 25, and 39 from Straw et al. (1989) are also indicated. The *MSX* source is represented by the dot-dashed small ellipse. No CS clump appears in the field of view. (*d*) Some of the sources selected to generate the color-color and color-magnitude diagrams of Fig. 4 are overlaid on the *K*-band image. [*See the electronic edition of the Supplement for a color version of this figure.*]

G351.16+0.70. The first estimate is based on the fluxes from IRAS 17165−3554. A total luminosity of $(4 \pm 1) \times 10^4$ $L_\odot$ yields a spectral type for the heating source later than B0 V (see Table 5). The second estimate is obtained by scaling the total luminosity given in Loughran et al. (1986) for the far-IR source NGC 6334-V (1.7×10^5 $L_\odot$ at 1.7 kpc) to our assumed distance of 1.2 kpc. We obtain a new $L_{\rm TOT} = 8.5 \times 10^4$ $L_\odot$, which yields an O8 V spectral type for the heating source.

The *IRAS* source is associated with the western lobe of the bipolar nebula (IRS 24). Since this is at the edge of the field of view of our images, we do not have photometric information on the stellar population to compare with the *IRAS* luminosity. The situation is different in the case of the far-IR source NGC 6334-V, which is clearly associated with the group of embedded near-IR sources 45, 33, 36, and 46 in our images. The spectral type inferred for the near-IR sources (one later than O6 V and three early- to mid-B V) is clearly earlier than the O9.5 V needed to explain the total luminosity associated with NGC 6334-V. Therefore, these near-IR sources may be contributing only partially to the heating of NGC 6334-V.

4.1.3. *G5.89−0.39*

G5.89−0.39 was classified by Wood & Churchwell (1989) as a shell-type UC H II region of diameter 5″. Kim & Koo (2001) found that the compact radio emission is located near the center of a 15′ extended ionized halo. Several OH, H$_2$O, and CH$_3$OH maser spots have been found in the region (Argon et al. 2000; Hofner & Churchwell 1996; Walsh et al. 1998). G5.89−0.39 is known to be associated with an outflow whose orientation has been found to be different (east-west, north-south, northeast-southwest) depending on the author and the tracer (Harvey & Forveille 1988; Cesaroni et al. 1991; Acord et al. 1997; Sollins et al. 2004).

Near-IR images at the seeing limit were obtained by Harvey et al. (1994). A detailed study of this UC H II region from near-IR to millimeter wavelengths was presented by Feldt et al. (1999). They show the first AO-assisted near-IR images of the region, with a resolution of 0″.4 in the *K* band.

Our new high-resolution near-IR images of G5.89−0.39 taken with ALFA are presented in Figure 5. The resolution of

Fig. 4.—(a) Color-color and (b) color-magnitude diagram for G351.16+0.70. Key to symbols and lines is given in Fig. 2. [*See the electronic edition of the Supplement for a color version of this figure.*]
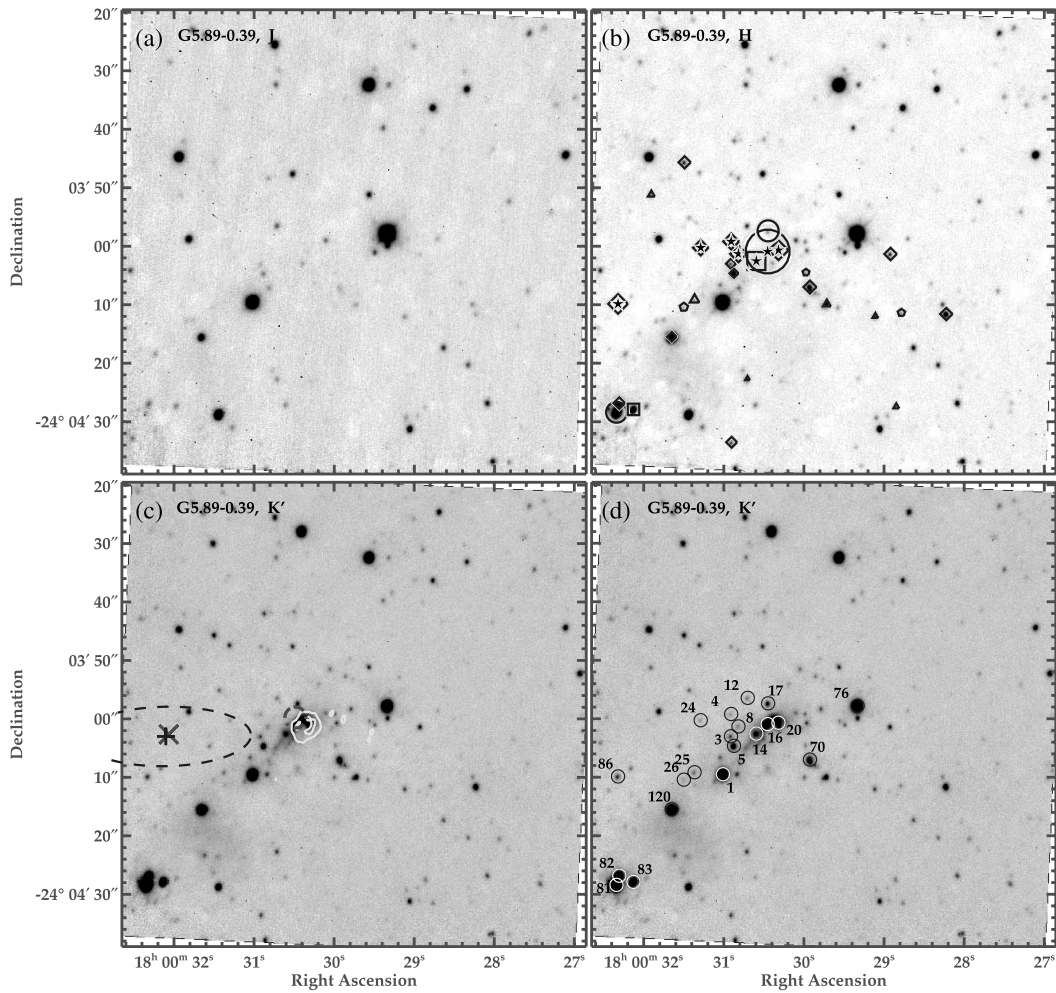
Fig. 5.—Near-IR images of G5.89−0.39. (a) *J*-band image. The gray scale varies from 14.5 mag arcsec^{-2} (*dark*) to 15.0 mag arcsec^{-2} (*white*). (b) *H*-band image. The gray scale varies from 12.8 to 13.0 mag arcsec^{-2}. See Fig. 1 for a key to the symbols. (c) *K′*-band image. The gray scale varies from 10.06 to 10.14 mag arcsec^{-2}. The white contours represent the radio emission at 2 cm. Contour levels are at 5, 15, and 25 σ. Symbols are the same as in Fig. 1. (d) Some of the stars selected to produce the color-color and color-magnitude diagrams of Fig. 6 are overlaid on the *K′*-band image. [*See the electronic edition of the Supplement for a color version of this figure.*]
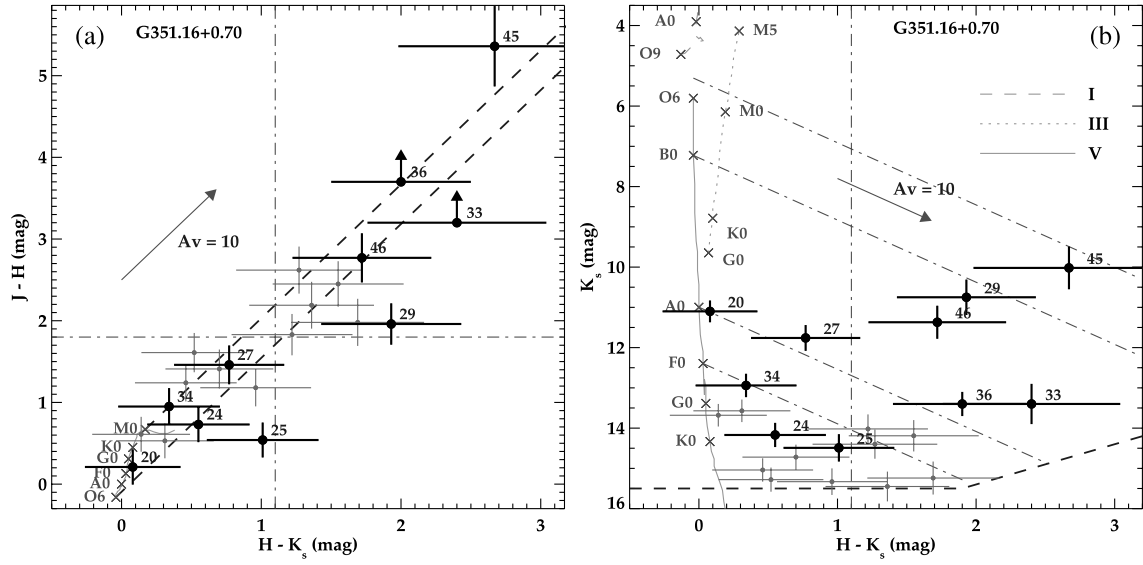
Fig. 6.—(a) Color-color and (b) color-magnitude diagram for G5.89−0.39. Key to symbols and lines is given in Fig. 2. [*See the electronic edition of the Supplement for a color version of this figure.*]
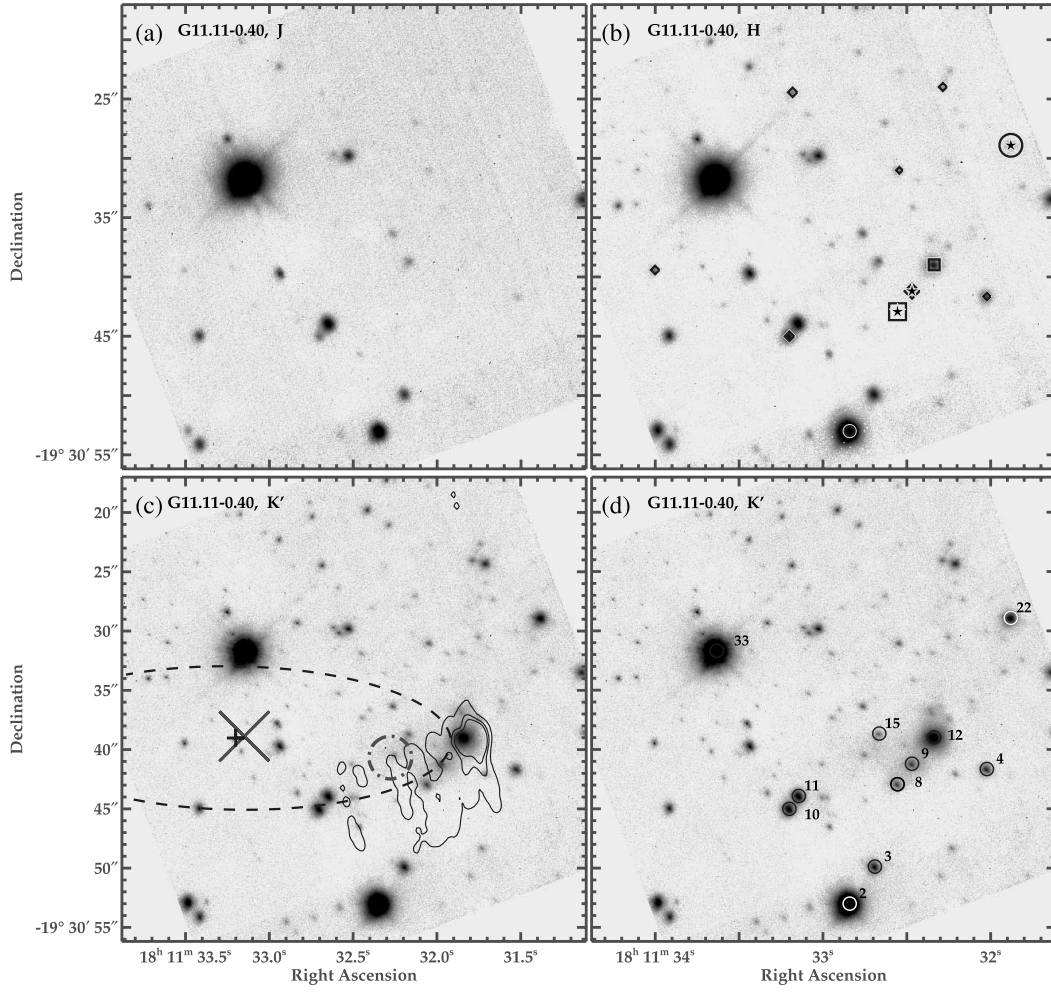
these data is comparable to that shown in Feldt et al. (1999; see also Henning et al. 2002). Our images show basically the same features as in Feldt et al. (1999). Nevertheless, we include them here for completeness.

The C-C diagram of this region is shown in Figure 6a (we use the same notation as in Feldt et al. 1999). Several sources appear to have $H - K_s$ excesses, although we focus our attention on sources 14, 16, 17, and 20, since they are very red and are located within or very close to the radio UC H II region. Source 14 appears as an unresolved core surrounded by an extended halo in our ALFA K_s-band image, while source 16 is only barely resolved. Source 17 is unresolved and source 20 appears to be clearly extended. In any case, we tried to assign a spectral type to all of them, by using the method described in § 3.2.1. Sources 14 and 17 appear to be late B V stars under ∼20 mag of visual extinction. The photometry of source 20 is consistent with a B5 V star under a $A_v \sim 25$ mag. Source 16 shows an extremely large excess, $H - K_s \sim 4$ mag, which yields a ∼F5 V spectral type, under the assumption that all the excess is in the K_s band. In the cases of sources 14, 17, and 20, giant spectral types from K III to G III are also possible based only on the photometry, but then these stars would lack any ionizing capabilities.

AO-assisted Fabry-Perot imaging shows that sources 14 and 20 are strong Brγ emitters, which would explain part of their IR excess (E. Puga et al. 2004, in preparation). The same data indicate that part of the emission in 16 is also due to Brγ. Recent K- and L′-band imaging with NAOS/CONICA at the VLT, with higher resolution and sensitivity than our ALFA images, indicate that source 16 actually contains a star of spectral type O5 V (Feldt et al. 2003), which is likely to be the ionizing star of the UC H II region owing to its location within the shell. Hence, our assumption of all the $H - K_s$ excess coming from the K_s-band appears to yield a far too late (F5 V) spectral type. Therefore, we adopt hereafter the spectral type inferred by Feldt et al. (2003), which scaled from their adopted distance of 1.9 kpc to our value of 2.6 ± 0.6 kpc, is ∼O3 V.

The spectral type of the ionizing star inferred from radio data is O8 V (see Table 5). The spectral type of a single star necessary to produce the *IRAS* emission is O7 V. Hence, in

G5.89−0.39, the near-IR spectral type of the best candidate for ionizing the H II region is earlier than the radio and *IRAS* spectral type. This is a common feature of almost all UC H II regions studied here, which will be discussed in §§ 4.2.3 and 4.2.4.

4.1.4. *G11.11−0.40*

This UC H II region, which was classified as irregular by Kurtz et al. (1994), has a well-defined core at 3.6 cm, with a halo that extends 10″ toward the southeast. It is associated with methanol maser emission (Walsh et al. 1997) and with high-velocity CO emission (Shepherd & Churchwell 1996).

The near-IR data of G11.11−0.40 presented here form part of the previous work shown in Henning et al. (2001). Our new improved photometry—we use a more appropriate model for the PSF (see § 2.5) and calibrate the photometry using the 2MASS PSC—yields H and K_s brightnesses 1 mag fainter than in Henning et al. (2001).

The near-IR morphology of this region is shown in Figure 7. We present the C-C and C-M diagrams in Figure 8. The most obscured sources within or near the radio-continuum emission are 8, 9, 12, and 22. Star 22, located some 10″ (0.25 pc) to the northeast of the UC H II region, also appears to suffer high extinction. The photometry of source 8 is consistent with an early A V star under a $A_v \sim 10$ mag. Sources 9 and 22 are consistent with late and early B V spectral types, respectively, with a visual extinction of ∼25 mag in both cases. Source 12, which is the closest to the radio peak, appears to be bluer than the reddened MS in the C-C diagram. The spectral type inferred from the C-M diagram is that of an O6 V with a visual extinction of ≳35 mag. Note that in this case no correction for the near-IR excess was made.

From the 2 cm flux density listed in Kurtz et al. (1994), we infer a log (N_L) = 47.8, i.e., a spectral type O9 V for the ionizing source. This spectral type is later than the O6.8 ZAMS obtained by Henning et al. (2001) because they used the peak flux density to derive the electron density and assumed this density to be uniform over a sphere of radius 0.2 pc. Here we do the calculation using the integrated flux density within a sphere of 0.2 pc (Kurtz et al. 1994). The spectral type inferred

Fig. 7.—Near-IR images of G11.11−0.40. (*a*) *J*-band image. The gray scale varies from 13.5 mag arcsec^{-2} (*dark*) to 17.7 mag arcsec^{-2} (*white*). (*b*) *H*-band image. The gray scale varies from 13.0 to 17.9 mag arcsec^{-2}. See Fig. 1 for a key to the symbols. (*c*) *K'*-band image. The gray scale varies from 12.4 to 17.2 mag arcsec^{-2}. The contours represent the radio emission at 3.6 cm. Contour levels are at 5, 15, and 25 σ. Symbols are the same as in Fig. 1. (*d*) Some of the stars selected to produce the color-color and color-magnitude diagrams of Fig. 8 are overlaid on the *K'*-band image. [*See the electronic edition of the Supplement for a color version of this figure.*]
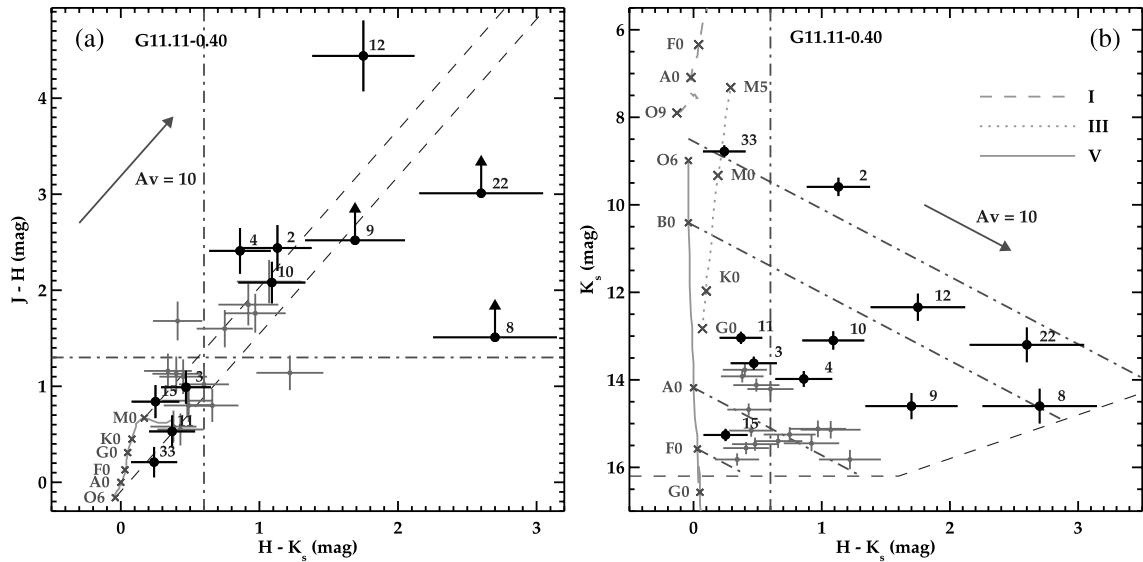
Fig. 8.—(*a*) Color-color and (*b*) color-magnitude diagram for G11.11−0.40. Key to symbols and lines is given in Fig. 2. [*See the electronic edition of the Supplement for a color version of this figure.*]
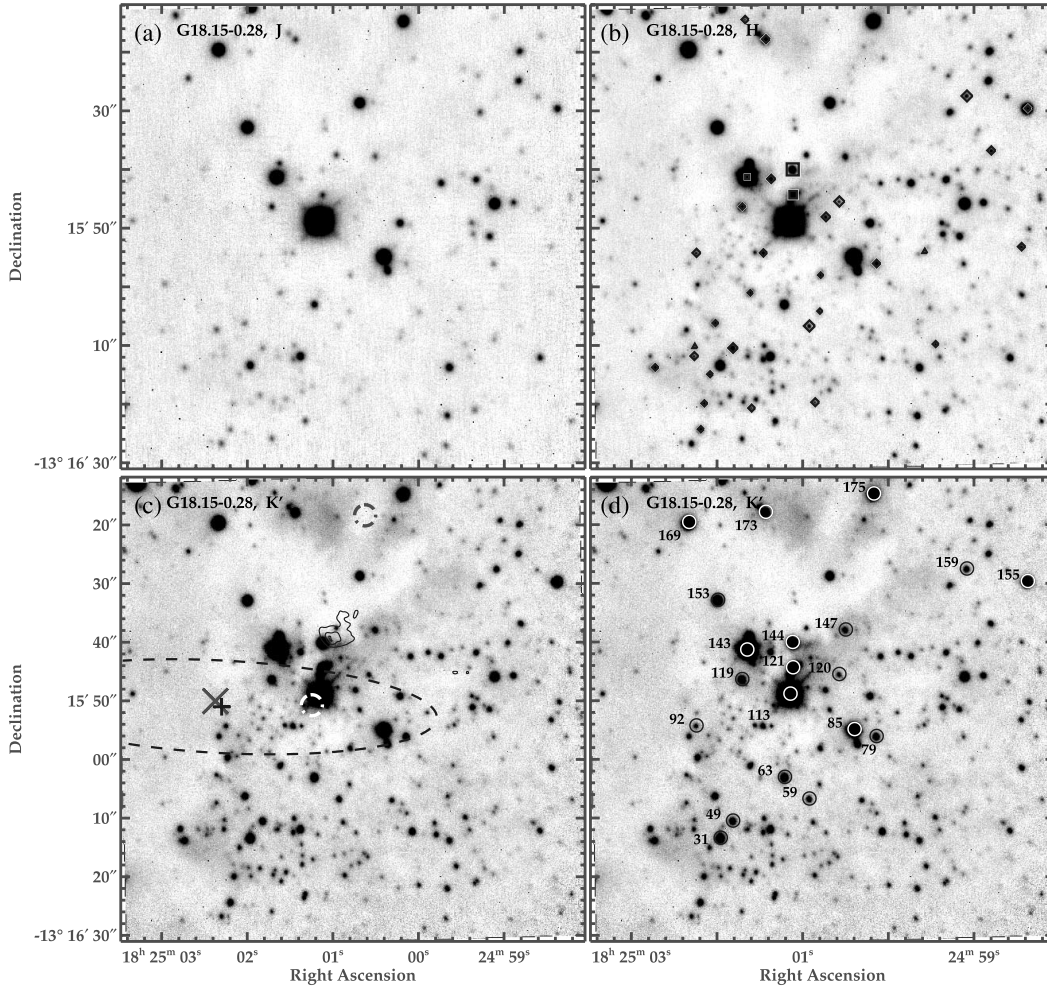
Fig. 9.—Near-IR images of G18.15−0.29. (a) J-band image. The gray scale varies from 14.8 mag arcsec^{-2} (*dark*) to 15.4 mag arcsec^{-2} (*white*). (b) H-band image. The gray scale varies from 13.6 to 13.9 mag arcsec^{-2}. See Fig. 1 for a key to the symbols. (c) K'-band image. The gray scale varies from 11.10 to 11.14 mag arcsec^{-2}. The contours represent the radio emission at 3.6 cm. Contour levels are at 3, 6, 9, and 12 σ. Symbols are the same as in Fig. 1. In this case, two *MSX* sources appear in the field of view (*clear and dark small dot-dashed circles*). (d) Some of the stars selected to produce the color-color and color-magnitude diagrams of Fig. 10 are overlaid on the K'-band image. [*See the electronic edition of the Supplement for a color version of this figure.*]

from the *IRAS* fluxes is O9 V, which is two spectral subtypes later that near-IR photometric spectral type of source 12. This UC H II region represents one of the instances where the near-IR colors of the best candidate to be the ionizing star indicate a spectral type earlier than the one inferred from both radio and *IRAS* fluxes.

4.1.5. G18.15−0.28

Little is known about this UC H II region classified as cometary by Wood & Churchwell (1989). The radio source lies at the edge of an extinction lane that covers part of the eastern region in the FOV of our near-IR images (see Fig. 9). The C-C and C-M diagrams (see Fig. 10) show that star 144, which is located within the radio UC H II region, is the most obscured source. The C-C diagram indicates reddening toward this source due to pure extinction, with no intrinsic IR excess. The spectral type obtained from the C-M diagram is that of an O6 V star under 30 mag of visual extinction. Sources 143 and 121, with spectral types O7 V and B0 V and visual extinctions of 10 and 20 mag, respectively, are also potential contributors to the ionization of the H II region.

Kurtz et al. (1994) infer a log (N_L) = 46.8 from the integrated flux density at 3.6 cm, which implies an B0.5 V spectral

type for the ionizing source. Therefore, in this case, it appears that the radio data underestimate by far the Lyman continuum photon rate associated with massive the stars detected with our near-IR photometry at and in the surroundings of the UC H II region. The *IRAS* fluxes yield an O7 V spectral type, which is in relatively good agreement with our near-IR photometry, unless we add up the luminosities from the brightest sources associated with the H II region (sources 121, 143, and 144).

4.1.6. G61.48+0.09

G61.48+0.09 is a complex of two UC H II regions located in the emission nebula Sh2-88B (Felli & Harten 1981). Here we focus our study on G61.48+0.09B, which itself has two components (see Fig. 11). B2 is the eastern region, classified as spherical or unresolved. B1, the western component, was classified as an extended cometary H II region, which is undergoing a champagne flow (Garay et al. 1994, 1998a, 1998b). The presence of molecular gas associated with these H II regions was inferred from CO and CS measurements (Schwartz et al. 1973; Blair et al. 1975). The velocity structure of the CO lines indicate the presence of several molecular outflows in G61.48+0.09 (Phillips & Mampaso 1991; White & Fridlund 1992).
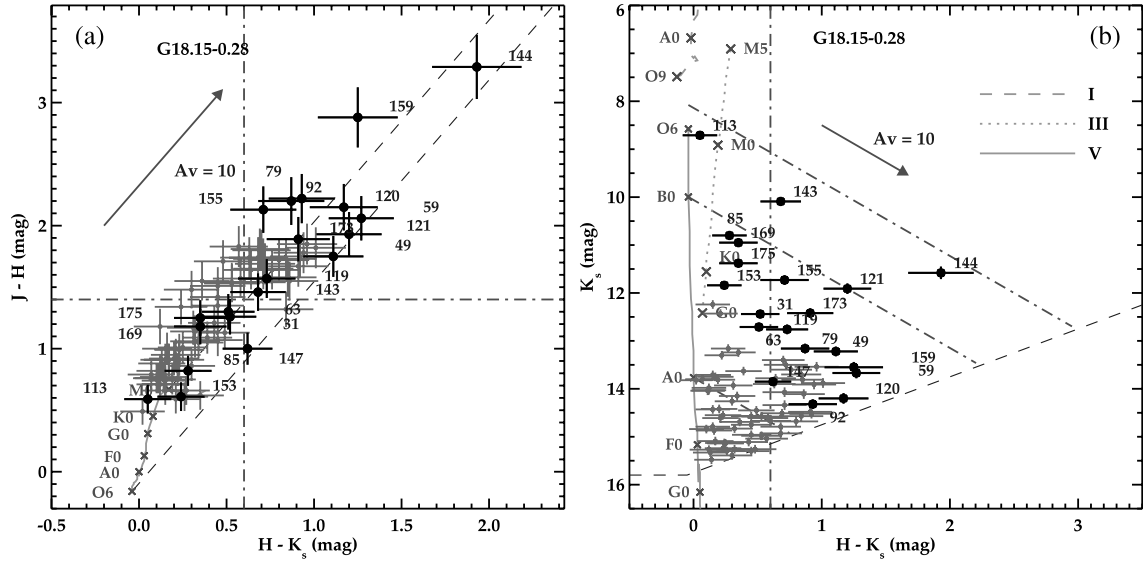
Fig. 10.—(a) Color-color and (b) color-magnitude for G18.15−0.29. Key to symbols and lines is given in Fig. 2. [*See the electronic edition of the Supplement for a color version of this figure.*]
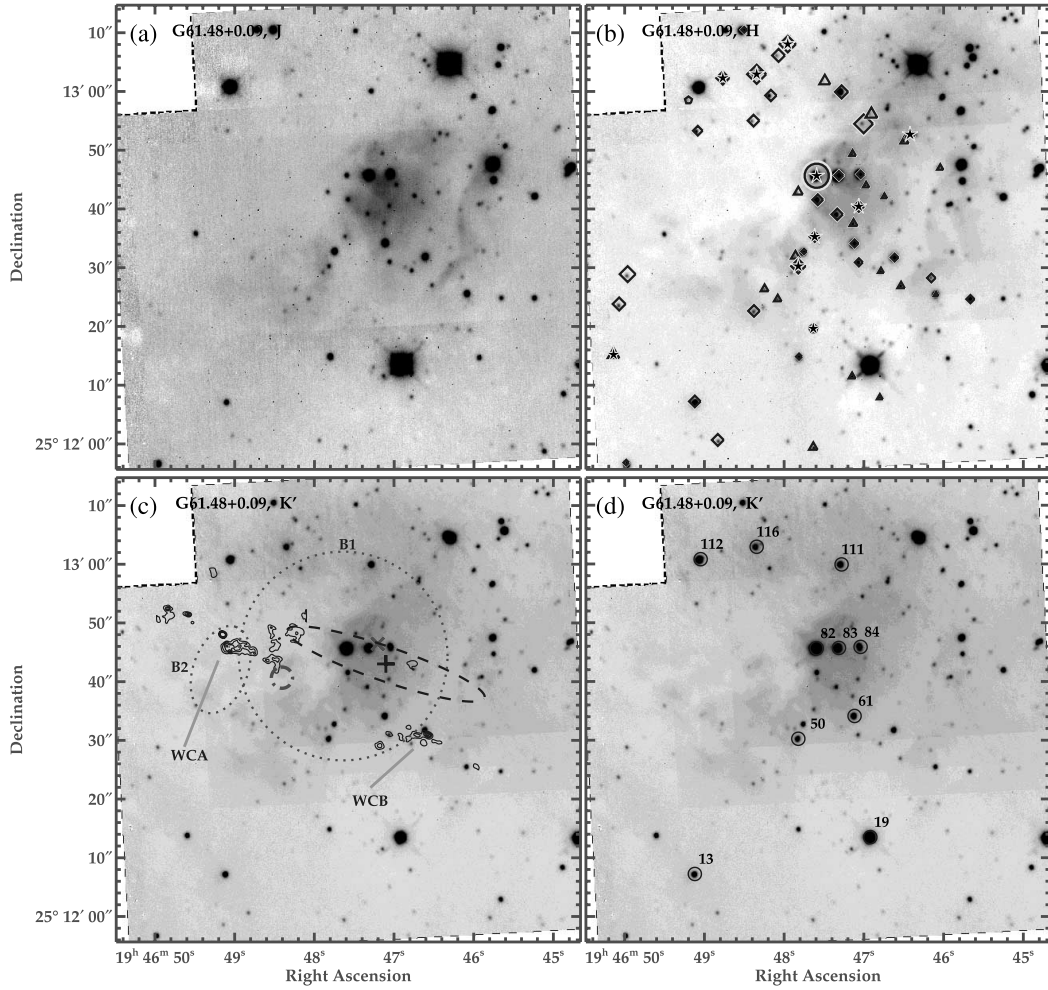

Fig. 11.—Near-IR images of G61.48+0.09. (a) *J*-band image. The gray scale varies from 14.8 mag arcsec^{-2} (*dark*) to 15.2 mag arcsec^{-2} (*white*). (b) *H*-band image. The gray scale varies from 13.3 to 13.6 mag arcsec^{-2}. See Fig. 1 for a key to the symbols. (c) *K'*-band image. The gray scale varies from 10.60 to 11.72 mag arcsec^{-2}. The contours represent the radio emission at 6 cm with the VLA in B configuration (Wood & Churchwell 1989). Contour levels are at 3, 6, 9, 12, and 15 σ. The radio sources denominated G61.48+0.09A and B in Wood & Churchwell (1989) are here labeled as WCA and WCB, respectively. Symbols are the same as in Fig. 1. In addition, the two thin dotted ellipses represent the radio components B1 and B2 from Garay et al. (1993). (d) Stars selected to produce the color-color and color-magnitude diagrams of Fig. 12 are overlaid on the *K'*-band image. [*See the electronic edition of the Supplement for a color version of this figure.*]
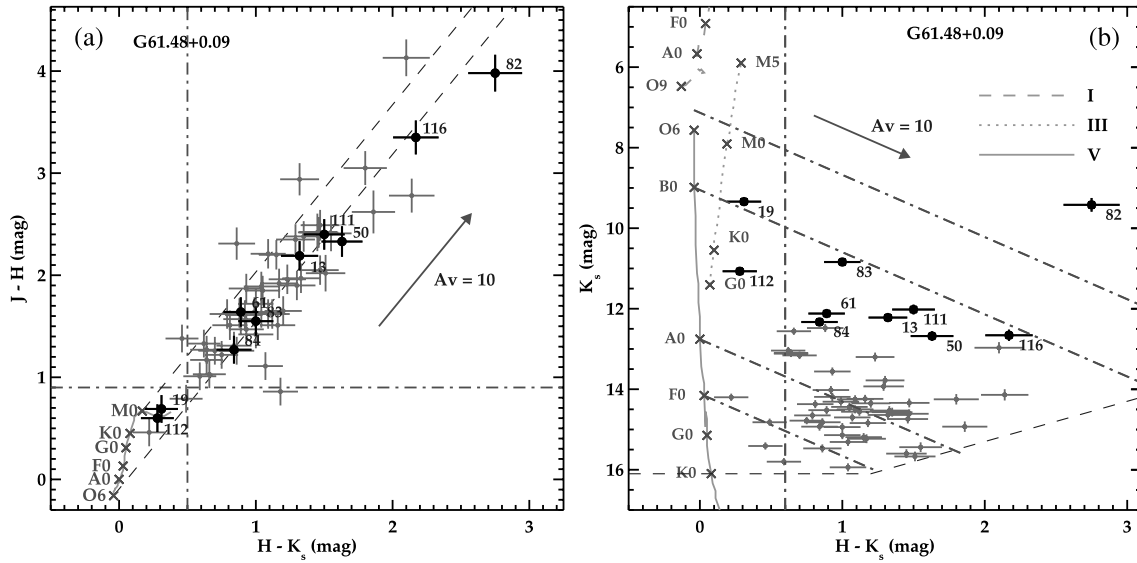
Fig. 12.—(a) Color-color and (b) color-magnitude diagram for G61.48+0.09. Key to symbols and lines is given in Fig. 2. [*See the electronic edition of the Supplement for a color version of this figure.*]

This region has been previously studied in the near-IR by Evans et al. (1981) and Deharveng et al. (2000), the latter with a resolution comparable to our AO-assisted images. In a separate paper, we (Puga et al. 2004) present a detailed description of this region, by combining AO-assisted near-IR polarimetry, narrowband imaging, and radio data with part of the photometry from this minicatalog.

In Figure 12, we present our C-C and C-M diagrams for G61.48+0.09. There is some slight discrepancy between our magnitudes (see Table 3) and the data shown in Deharveng et al. (2000), although both sets of data agree within the errors. Stars 82 and 83 appear to be the main contributors to the ionization, owing to their high luminosity, proximity to the radio peak, and degree of obscuration. From our photometry, we infer an O9 I spectral type for star 82 and a B0 V type for star 83, under A_v-values of 35 and 15 mag, respectively. For this estimate, we have subtracted 0.01 mag from the K_s magnitude of source 82 due to Brγ emission (Puga et al. 2004). The supergiant nature of star 82 is reinforced when its L' magnitude is also considered (Puga et al. 2004).

The radio data yield different values for the number of Lyman continuum photon rate depending on which assumptions are made for the geometry of the radio-emitting region. In the case of the B2 component, if we scale the value of N_L given in Wood & Churchwell (1989)[5] [log (N_L) = 46.2 at 2.0 kpc] to a distance of 2.7 kpc, we obtain a spectral type B1 V for the ionizing source (see Table 5). For this estimate, Wood & Churchwell (1989) used the integrated flux and size at 6 cm measured with the VLA in B configuration. Deharveng et al. (2000), however, based their calculation on radio data taken at lower spatial resolution (Felli & Harten 1981; Garay et al. 1993). They infer a log (N_L) = 48.4 and log (N_L) = 47.4 at a distance of 2.4 kpc for components B1 and B2, respectively. These Lyman photon rates scaled to a distance of 2.7 kpc imply spectral types for components B1 and B2 of ∼O8 V and ∼B0 V, respectively. Furthermore, Puga et al. (2004) show that different (and equally valid) assumptions on the geometry of the ionized

region yield variations in the Lyman photon rate of up to 1 order of magnitude. The spectral type inferred from the *IRAS* source associated with G61.48+0.09 is an O7.5 V.

Summing up, the spectral type for the hottest star derived from our near-IR photometry (∼O9 I) is one luminosity class higher than the radio spectral type of component B1 (∼O9 V) and also two spectral subtypes earlier than the radio spectral type of component B2 (∼B1 V). An O9 I star is 3.5 times more luminous than the luminosity inferred from the *IRAS* fluxes. This difference may be explained if a population of stars hidden in our near-IR images are the actual ionizing sources of this complex H II region, as well as the heating stars of the *IRAS* source. Part of this population may have already started to show up in recent L'-band NACO observations (Puga et al. 2004). An anisotropic dust distribution, which would be only partially heated by the detected near-IR population, may also cause this difference.

4.1.7. *G70.29+1.60 (K3-50A)*

G70.29+1.60 is a well-studied UC H II region, classified as a compact radio shell by Turner & Matthews (1984) and as a core-halo source by Kurtz et al. (1994). G70.29+1.60 is the brightest and youngest of a complex of four radio sources (K3-50A to D) spread over an area of 3′.5 (i.e., 8 pc at the adopted distance of 8.2 kpc). G70.29+1.60 is coincident with a 10 μm peak (Wynn-Williams et al. 1977), and also with a CS core (Bronfman et al. 1996).

Studies of radio-recombination line emission suggest the presence of moving ionized material (e.g., Rubin & Turner 1969; Wink et al. 1983; Roelfsema et al. 1988; DePree et al. 1994). In particular, DePree et al. (1994) show that G70.29+1.60 is undergoing a high-velocity bipolar outflow in the northwest-southeast direction. Based on CO observations, Phillips & Mampaso (1991) infer a bipolar outflow in the northeast-southwest direction.

Seeing-limited near-IR imaging was performed by Howard et al. (1996). They obtained an extinction map of the region as well as reinforced the idea of an outflow of ionized gas with a roughly north-south orientation. Okamoto et al. (2003) did a detailed study of the stellar population and ionization structure

---

[5] Note that source G61.48+0.09A in Wood & Churchwell (1989) corresponds to source B2 in the notation of Garay et al. (1998a), which we adopt.

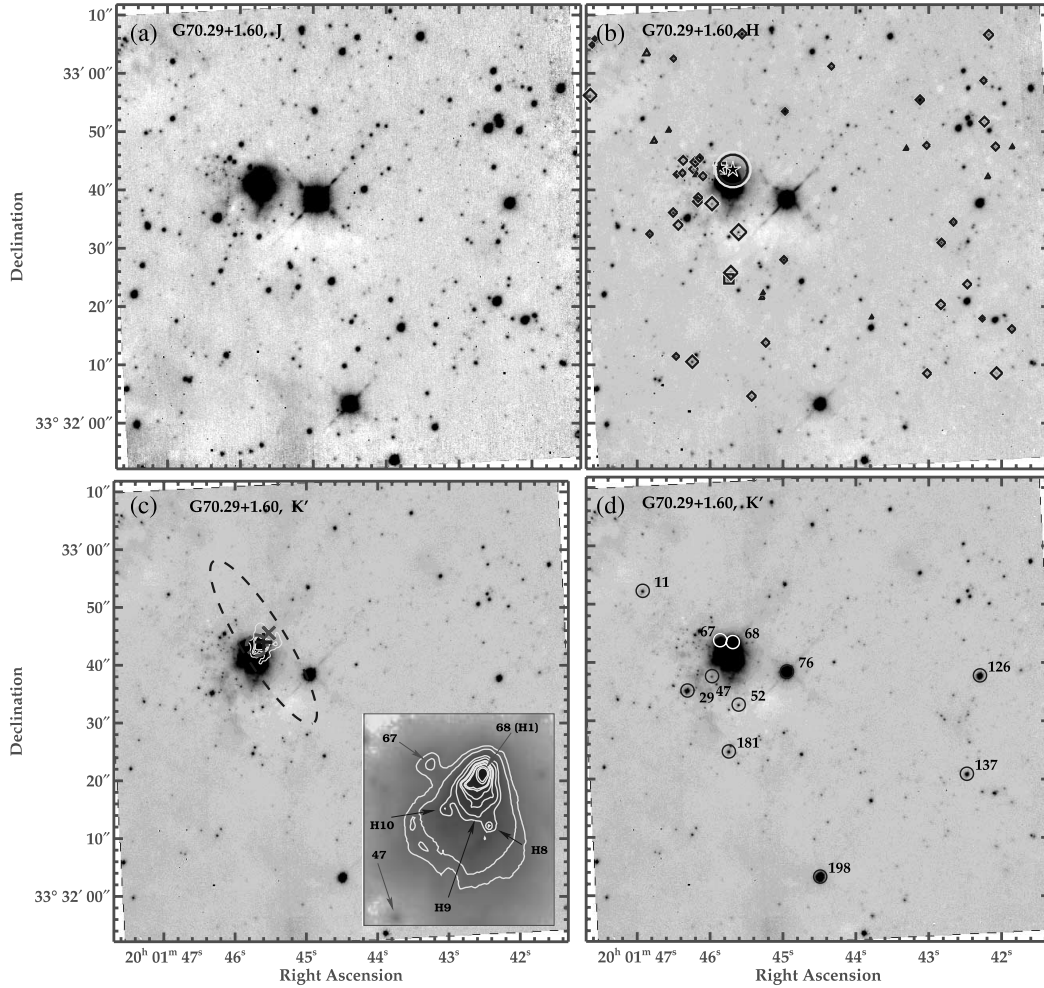Fig. 13.—Near-IR images of G70.29+1.60. (*a*) *J*-band image. The gray scale varies from 14.5 mag arcsec^{-2} (*dark*) to 14.9 mag arcsec^{-2} (*white*). (*b*) *H*-band image. The gray scale varies from 13.2 to 13.8 mag arcsec^{-2}. See Fig. 1 for a key to the symbols. (*c*) *K'*-band image. The gray scale varies from 10.6 to 10.8 mag arcsec^{-2}. The contours represent the radio emission at 2 cm. Contour levels are at 5, 15, and 25 σ. Symbols are the same as in Fig. 1. In this case, the *MSX* source, the center of the *IRAS* ellipse, and the CS core coincide within the errors. The inset shows a close up of the central $7\rlap{.}''5 \times 8\rlap{.}''5$ of G70.29+1.60. A log-log scale was used to show both, the low-level structure of the nebula as well as the point sources. Labels show some of the sources from Hofmann et al. (2004) (H1, H8, H9, H10) and some of the stars studied in our photometry. Note that H1 and H10 correspond with sources OKYM3 and OKYM4 in Okamoto et al. (2003), respectively. (*d*) Some of the stars selected to produce the color-color and color-magnitude diagrams of Fig. 14 are overlaid on the *K'*-band image. [*See the electronic edition of the Supplement for a color version of this figure.*]

in the region, based on near- and mid-IR imaging and spectroscopy at a resolution of $\sim0\rlap{.}''4$ with the Subaru telescope. More recently, Hofmann et al. (2004) studied the morphology of the central $1'' \times 1''$ with a resolution of $\sim0\rlap{.}''1$ using speckle imaging at the SAO 6 m telescope in Russia.

In Figure 13, we present our ALFA images of G70.29+1.60 with a resolution of $0\rlap{.}''22$ and a Strehl ratio of 0.14 in the *K'*-band. The morphology of the near-IR nebula is similar to that found by Okamoto et al. (2003) and Hofmann et al. (2004) (see the inset in Fig. 13*c*). Some of the sources labeled in Figure 13*d* (29, 47, 52, 67, and 68) are clearly cross-identified with sources in Figure 3 in Okamoto et al. (2003) and Figures 1 and 2 in Hofmann et al. (2004). We also encounter near-IR point sources coincident with the position of the 11.4 μm peaks OKYM 3 and OKYM 4. In particular, our source 68 is coincident with OKYM 3, which is located at the center of the radio-emitting source. No photometry of the near-IR source associated with OKYM 4 was possible, owing to its location, which is highly embedded in the bright near-IR nebulosity.

Sources 67 and 68 are the most likely ionizing sources, based on their location with respect to the radio peak and their

position in the C-C and C-M diagrams (Fig. 14). Source 67 is consistent with a B0 V star under a visual extinction of ~20 mag. Detailed inspection of the *K'* band image shows that this source is elongated in the northwest-southeast direction. Source 68 appears to be extremely overluminous in the C-M diagram. It has an excess of ~1.5 mag in the $H - K_s$ color. Even if we assume that this excess is mainly in the K_s band, the high luminosity of source 68 can only be explained if it is a supergiant of spectral type later than A0 I under ~30 mag of visual extinction. However, because of the strong nebular contamination within the region of $2''$ around 68, this spectral type estimate should be taken with caution. Besides, a star with such a spectral type would not contribute to the ionization of the H II region. Further high-resolution spectroscopy in the near-IR is required to find photospheric lines associated with star 68, and therefore, to determine whether this source is actually a star, and if this were the case, to determine its spectral type.

In any case, we can compare the expected stellar ionizing population from published radio and IR data with the one suggested by our near-IR photometry. Kurtz et al. (1994) estimated a log $(N_L) = 49.3$ and Martín-Hernández et al.
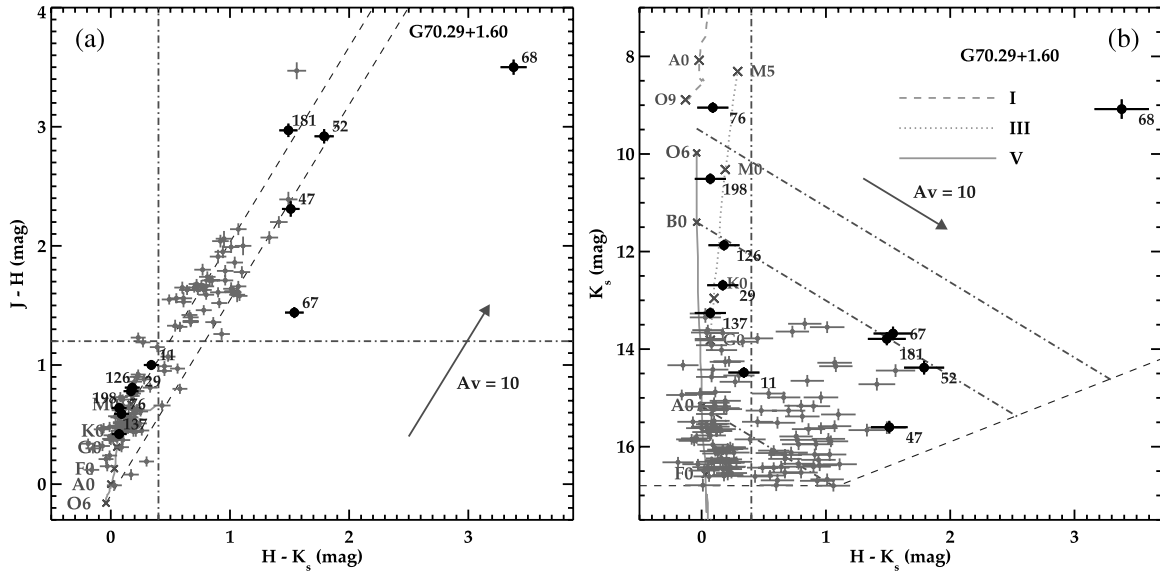
Fɪɢ. 14.—(a) Color-color and (b) color-magnitude diagram of G70.29+1.60. Key to symbols and lines is given in Fig. 2. [See the electronic edition of the Supplement for a color version of this figure.]

(2002) obtained a log (N_L) = 49.1. If we scale these values to a distance of 8.2 kpc, we obtain an O5 V spectral type for a single ionizing star (Smith et al. 2002). This value, based on 2 cm interferometry, is in good agreement with the O6 V–O9 V spectral type inferred by Okamoto et al. (2003) from modeling of the ionization structure of the mid-IR source OKYM 3 (i.e., our source 68). The Lyman photon rate of G70.29+1.60 [log (N_L) = 49.2] can also be produced by an O3 I star, which would be in somehow better agreement with the luminosity inferred from our near-IR photometry.

Regarding the other mid-IR source with near-IR counterpart (OKYM 4), Okamoto et al. (2003) obtained a spectral type between B0 V and O9 V. This source (star 10 in Hofmann et al. 2004) is not included in our C-C and C-M diagrams because it was barely detected in the K' image and not detected at all at shorter wavelengths.

Regarding the total luminosity of G70.29+1.60, its *IRAS* fluxes indicate a log ($L/L_\odot$) ∼ 6.30. This cannot be delivered by a single dwarf star [note that log ($L/L_\odot$) = 6.03 for an O3 V star], but it is plausible for a single supergiant star [log ($L/L_\odot$) = 6.27 for an O3 I]. Even source 68, which may be an A9 I star, would be not luminous enough. This may be due to the presence of a population of hot stars, hidden at near-IR wavelengths, which would be contributing to the *IRAS* emission. Some members of this population could correspond to the mid-IR sources detected by Okamoto et al. (2003).

4.1.8. G77.96−0.01

This UC H ɪɪ region, located at a distance of 4.2 kpc from the Sun, was classified as irregular based on its morphology at radio wavelengths (Kurtz et al. 1994). Its subarcsecond morphology in the near-IR has not been previously studied.

In Figure 15, we present the ALFA *J*, *H*, and *K'* images of this region. The radio UC H ɪɪ region is coincident with a bright near-IR nebulosity in the northeastern region of our FOV. Inspection of the 2MASS K_s image over a field of view 5 times larger than the one shown in Figure 15 illustrates how the southern part of this reflection nebula is actually a bright knot of a long *snakelike* nebula extending for ∼3′ toward the northeast and west.

Our C-C and C-M diagrams (Fig. 16) indicate two likely candidates that may be ionizing the H ɪɪ region, sources 7 and 9, which are situated within 5″ (i.e., 0.1 pc) of the UC H ɪɪ region and within the near-IR nebulosity. They have spectral types ∼O8 V and B2 V, respectively, both showing an extinction of about 10 mag in the visual. At the location of the radio peak, we find source 11. Its extinction is high enough to yield only an upper limit for the *J* magnitude. Its $H − K_s$ color shows an excess of ∼1 mag. Its spectral type after removing, this excess is that of an early B V star. Another possibility is that this source may simply be an unresolved externally ionized knot. Source 45 is also located within the near-IR nebulosity. The spectral type inferred for this source is O8 V, with a visual extinction of 10 mag. Therefore, two O8 V stars and two early B V stars appear to be the best candidates for ionizing sources of this region.

We estimate a log (N_L) = 46.5 from the integrated flux and size of the G77.96−0.01 radio source at 2 cm (Kurtz et al. 1994). This value implies a B1 V spectral type for the ionizing source, which is later than the spectral types inferred from the near-IR photometry. For the *IRAS* source associated with G77.96−0.01, we find a spectral type O8 V, which is in good agreement with that of the hottest star in the near-IR images.

4.2. General Properties

After having discussed each source individually, in this section we focus on the general features of our near-IR data and compare them with published data at other wavelengths.

4.2.1. Mass Function

We note that all C-C diagrams show a gap in the distribution of stars along the band that represents the extincted MS. This gap appears to be clear in G70.29+1.60, but not so well defined in G18.15−0.28, where the photometric errors are larger. In any case, we have used this gap as a criterion to differentiate between foreground stars and stars that are likely to be associated with the H ɪɪ region. To quantify this distinction, we have defined two $J − H$ and $H − K_s$ color cutoffs. Stars with colors above the cutoffs are assumed to be at the same distance as the UC H ɪɪ region. The spread of these stars along the extinction
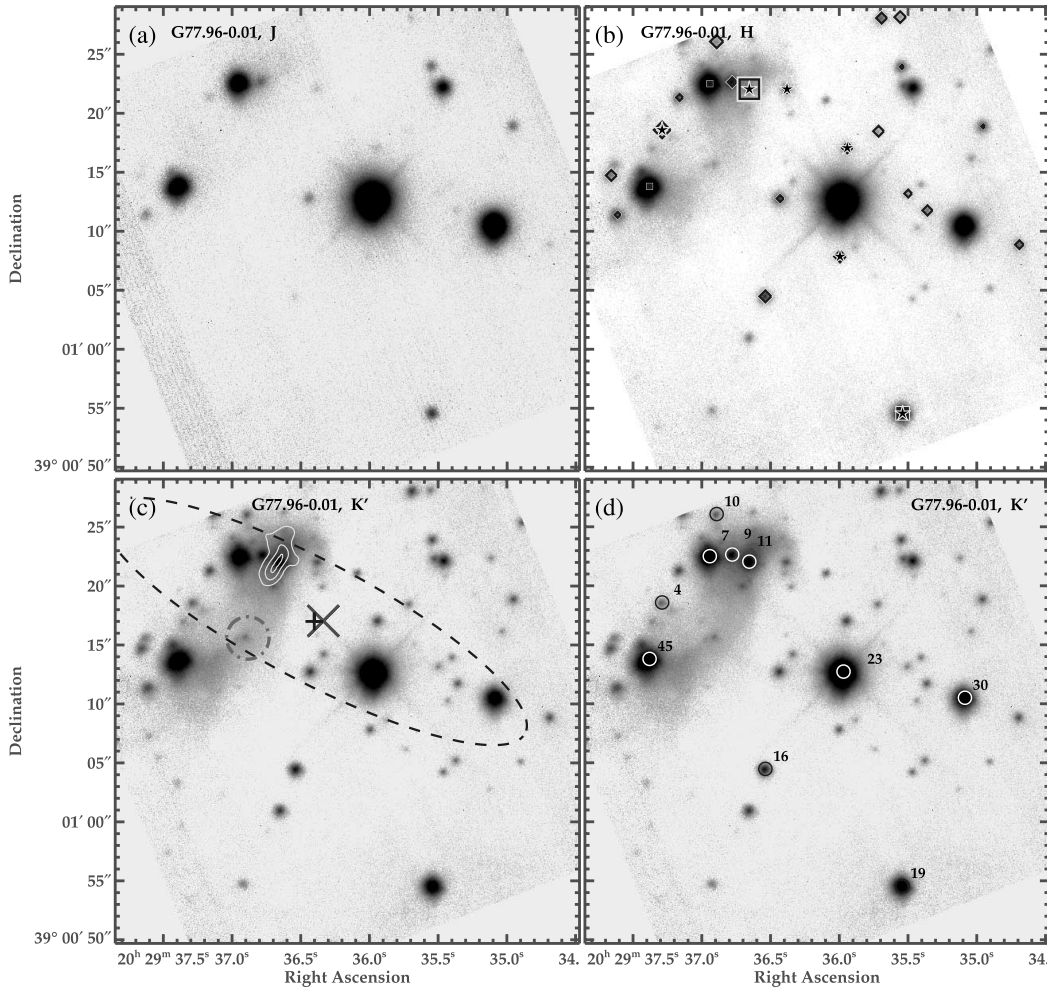
Fig. 15.—Near-IR images of G77.96−0.01 with a resolution of 0″.5. (*a*) *J*-band image. The gray scale varies from 13.4 mag arcsec^{-2} (*dark*) to 17.4 mag arcsec^{-2} (*white*). (*b*) *H*-band image. The gray scale varies from 12.8 to 17.4 mag arcsec^{-2}. See Fig. 1 for a key to the symbols. (*c*) *K*′-band image. The gray scale varies from 11.9 to 16.8 mag arcsec^{-2}. The contours represent the radio emission at 3.6 cm. Contour levels are at 2, 6, and 9 σ. Symbols are the same as in Fig. 1. (*d*) Some of the stars selected to produce the color-color and color-magnitude diagrams of Fig. 16 are overlaid on the *K*′-band image. [*See the electronic edition of the Supplement for a color version of this figure.*]

band in the C-C diagram is considered to be due to local variations of the dust and dense gas distribution at and in the surroundings of the H II region. Color cutoffs for each region are listed in Table 6 and are shown as dot-dashed lines in the C-C diagrams. In Table 6, the *typical* extinction toward stars above the cutoff is listed for each region. This typical extinction was estimated from visual inspection in the C-C diagram of the centroid of the stars along the reddened MS, which are also above the cutoffs. This value is slightly larger than the extinction associated with the point in the C-C diagram where both cutoff lines intersect. The expected line-of-sight foreground extinction to each source can be estimated from their distance. If we use $A_v/d = 0.68$ mag kpc^{-1} from Bohlin et al. (1978) (where d is the distance), the expected foreground extinction ranges from 0.8 mag for G351.16+ 0.70 to 5.6 mag for G70.29+1.60. In all UC H II regions, this foreground extinction is consistent with (i.e., smaller than) the A_v inferred from the color cutoffs in our C-C diagrams.

From the C-M diagrams, we counted the number of stars for each spectral type located above the color cutoffs, which we assume to be at the same distance as the UC H II region. The star counts are shown in columns (4)–(8) of Table 6. For the lower end of the mass function, the completeness is clearly not

reached, since MS stars later than A are normally below the detection limit. However, we can compare the ratio of the number of O-type stars to the number of B-type stars ($N_{O/B}$), with the expected ratio from a theoretical expression for the IMF, since the completeness should be better in the upper end of the mass spectrum. In this mass range, the exponent of the IMF is −1.3 (Miller & Scalo 1979), yielding a ratio $N_{O/B} \sim$ 0.16. For the regions that have high stellar counts, i.e., G18.15−0.28, G61.48+0.09, and G70.29+1.60, the $N_{O/B}$ is 0.11, 0.03, and 0.07, respectively. The agreement between these values and the IMF is reasonably good for G18.15−0.28, but fails for G61.48+0.09 and G70.29+1.60. This may be an indication that not all UC H II regions contain very massive O stars. However, before any robust conclusion on the IMF can be drawn, deeper observations at higher resolution and also at longer wavelengths are needed to achieve a higher degree of completeness and to unveil very obscured stars.

4.2.2. Near-IR Ionizing Sources

We have made an attempt to identify, using near-IR photometry, the main ionizing stars for each UC H II region. Column (3) of Table 5 shows that for all regions we have found at least one source with a spectral type early enough to
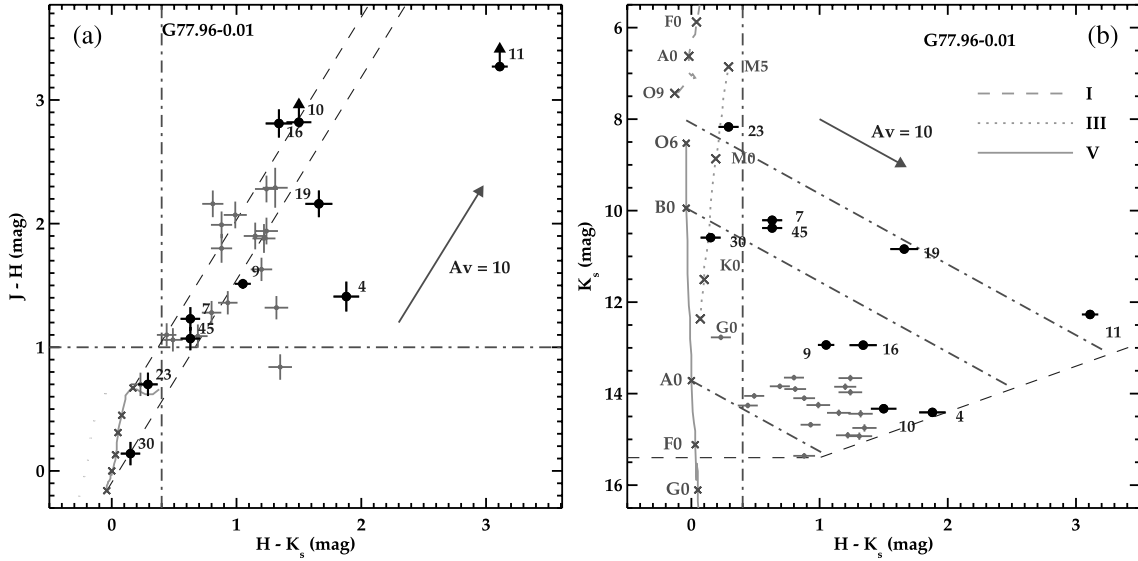
FIG. 16.—(*a*) Color-color and (*b*) color-magnitude diagram of G77.96−0.01. Key to symbols and lines is given in Fig. 2. [*See the electronic edition of the Supplement for a color version of this figure.*]

be capable of ionizing an H II region. However, the question of whether this source(s) is the actual ionizing star(s) of the radio UC H II region is still to be answered. Our identification has the advantage of the high resolution delivered by AO imaging and the relative transparency of dust and dense gas at near-IR wavelengths. It is certainly true that these sources identified as ionizing stars are unresolved and show high extinction ($A_v > 30$ mag) and/or intrinsic IR excess, which indicate their youth and possible relation with the H II region. In all cases but G351.16+0.70 and G61.48+0.09, their position coincides with that of the radio peak that defines the UC H II region (see *H*-band images in Figs. 1–15). Even the two exceptions can be explained. G351.16+0.70 appears to be simply a knot that is part of a much larger ionization shell (1′ radius, i.e., 0.4 pc), so it is not surprising that no stars are found at the radio peak. G61.48+0.09 appears to be a rather evolved compact H II region, which shows several separated peaks at high-interferometric resolution and extends for over 30″ (i.e., 0.4 pc) in low-resolution radio maps.

We have used C-C and C-M diagrams to spectral classify the possible ionizing sources and other sources associated with the UC H II regions. Our photometric spectral classification, however, is not without problems. UC H II regions appear to be rather complex in the near-IR at subarcsecond scales, showing some degree of crowding as well as spatially variable background owing to the presence of extended nebulosity. This makes it difficult to calculate magnitudes accurately. To solve these problems at least partially, we have used PSF fitting photometry, which should reduce the contribution to the stellar flux due to barely resolved stellar neighbors and due to the presence of a spatially variable background. The possibility that some of the sources identified as single stars are multiple systems or unresolved emission line knots cannot be completely discarded owing to the relatively large distances (between 1.2 and 8.2 kpc) to these UC H II regions. The high resolution delivered by AO though (between 0″.13 and 0″.55, which turns into projected separations of ∼1000 AU), alleviates this possibility. Other typical problems associated with the photometric spectral classification are temporal variability in young stars, undetermined photometric excesses due to unresolved dust

emission, scattering, accretion disks, and uncertainties in the distance and in the extinction.

4.2.3. *Comparison with Radio Sources*

In most of the UC H II regions, the spectral type of the ionizing source obtained from radio-continuum interferometry is a few subtypes later than the spectral type inferred from our near-IR photometry. One possible explanation is that part of the ionizing flux produced by the sources detected in our near-IR images is being absorbed by dust in the region. If the radio free-free emission is optically thick, radio interferometry may also be underestimating the Lyman continuum. A clumpy density distribution within the UC H II region can also yield an underestimate for the N_L. One additional problem is the fact that radio interferometry is sensitive only to high spatial frequencies. If the UC H II region is a mere density enhancement within a larger undetected extended halo of ionized gas, the total N_L associated with the full-size H II region may be more compatible with the stellar content inferred from our near-IR photometry. Extended halos of ionized gas are known to exist in a number of UC H II regions (e.g., Kurtz et al. 1999; Kim & Koo 2001). Kim & Koo (2001) find typical ratios ≳10 between H I 21 cm single dish fluxes and VLA fluxes. Even though the higher continuum flux in the single-dish observations comes from a larger ionized gas volume, the spectral types inferred from single-dish observations are 4 times earlier than those inferred from radiointerferometry. Such kind of differences would help to reconcile the spectral types inferred from the near-IR stellar population with those inferred from radio measurements.

A spectral type classification based on radio data also has the problem that it depends on the stellar models adopted. Table 5 shows that for a given N_L, the spectral types inferred using the models in Smith et al. (2002) are earlier than the spectral types inferred from the models in Vacca et al. (1996). This is mainly due to the more realistic approach of Smith et al. (2002), by using models that include stellar winds, spherical geometry, and line blanketing by metals (Pauldrach et al. 2001). Even though the line blanketing does not affect the N_L-T_{eff} relation (see Mokiem et al. 2004), it does affect the T_{eff}–spectral type relation. This trend toward earlier spectral types for a given T_{eff}

TABLE 6

STAR COUNTS

Object (1)	$(H - K_s)_c{}^{\mathrm{a}}$ (mag) (2)	$(J - H)_c{}^{\mathrm{b}}$ (mag) (3)	>O3 V[c] Number (4)	O3 V–O9 V Number (5)	B0 V–B9 V Number (6)	A0 V–A9 V Number (7)	<A9 V[c] Number (8)	Ex.[d] Number (9)	$A_v{}^{\mathrm{e}}$ (mag) (10)
G309.92+0.48	0.9	1.6	3	2	5	...	...	1	16
G351.16+0.70	1.1	1.8	0	1	4	2	3	3	19
G5.89-0.39	0.6	1.3	2	2	14	6	3	7	17
G11.11-0.40.........	0.6	1.3	2	2	7	0	...	3	16
G18.15-0.28	0.6	1.4	0	3	27	2	...	0	12
G61.48+0.09	0.5	0.9	1	0	30	20	2	10	15
G70.29+1.60	0.4	1.2	1	2	41	10	...	2	14
G77.96-0.01	0.4	1.0	0	4	20	0	...	6	14

[a] Cutoff in the $H - K_s$ color.
[b] Cutoff in the $J - H$ color.
[c] ">O3 V" means earlier than O3 V and <A9 V means later than A9 V.
[d] Number of stars from cols. (4) to (8) that show intrinsic excess in the C-C diagram.
[e] Typical visual extinction(s) toward stars with colors above the cutoffs inferred from the C-C diagrams. The A_v-value for each region is calculated for a *typical* star above the cutoff, which is slightly larger than the A_v-value for the cutoff itself.

is also seen when the CMFGEN models (Hillier & Miller 1998), which also include stellar winds and line blanketing, are used (see Martins et al. 2002). Therefore, the use of models including a more realistic physics helps to reconcile the near-IR photometric spectral-type classification of the possible ionizing stars and the classification inferred from radio continuum measurements.

4.2.4. *Comparison with IRAS Sources*

We find that, in general, the luminosity inferred from the *IRAS* sources associated with the UC H II regions is lower than what it is expected from the analysis of the stellar population based on our near-IR photometry (see Table 5). The spectral classification based on the luminosity inferred from *IRAS* fluxes is also model dependent. In this case, Table 5 shows that for a given L_{TOT}, the model grid by Smith et al. (2002) yields spectral types slightly earlier than the grid by Vacca et al. (1996). This difference, even if it is only of half to one spectral subclass, tends to reconcile the *IRAS*-based and photometric spectral types. In any case, even with the use of the grid by Smith et al. a discrepancy of over one spectral subclass still exists between the *IRAS* and near-IR spectral types for most of the sources.

One possible explanation for this general discrepancy between *IRAS* and near-IR luminosities is that the stellar population that shows up at near-IR wavelengths is already in a rather advanced evolutionary stage, and therefore it is not the major contributor to the mid- and far-IR flux. It is likely that a more embedded population of stars that would show up at longer wavelengths is actually producing the majority of the mid- and far-IR flux. This may be the case in G61.48+0.09 and G70.29+1.60, where studies at wavelengths longer than 2 μm appear to show part of this population (Puga et al. 2004 and Okamoto et al. 2003, respectively). AO-assisted observations with 8 m class telescopes at wavelengths longer than 2.2 μm can provide the sensitivity and resolution necessary to pinpoint this possible embedded stellar population (see Feldt et al. 2003).

Alternatively, if the dust spatial distribution is anisotropic, it is possible that the stars seen in the near-IR are actually heating, but only partially, the dust producing the emission detected in the mid- and far-IR by *IRAS*. The radiation field associated with the *IRAS* source in this case will no longer be spherically symmetric, making luminosity estimates based on reprocessed radiation extremely geometry dependant. Stellar radiation will leak out and leave no sign at mid- and far-IR wavelengths, yielding luminosities associated with the *IRAS* source smaller than those associated with the near-IR population.

A very simple calculation by dividing the luminosities inferred from the *IRAS* fluxes and the luminosities associated with the spectral types inferred from our near-IR photometry can be used to obtain a rough estimate of the fraction of radiation that must be absorbed by the dust causing the *IRAS* emission. We find that the fraction of absorbed radiation varies from only 10% for G351.16+0.70 to as high as ∼85% for G309.92+0.48. It is ∼25% for G5.89−0.39, G11.11−0.40, and G61.48+0.09 B1, and between 55% and 65% for G77.96−0.01 and G18.15−0.28. For G70.29+1.60, the *IRAS* luminosity is higher than the near-IR luminosity. Interferometry in the mm and submillimeter range to trace the distribution of dust at a similar resolution to that of near-IR imaging, complemented with radiative transfer modeling will be necessary to further investigate this calculation.

4.2.5. *CS Cores and MSX Sources*

All UC H II regions but G351.16+0.70 are associated with a CS core listed in Bronfman et al. (1996). Their position

accuracy is ∼3″. Bronfman et al. (1996) observed these dense clumps in the millimeter CS(2−1) transition. They have sizes slightly higher than their instrumental beam size of 40″−50″. The centroids of the CS cores are normally coincident with the *IRAS* peaks. The typical separation between the near-IR ionizing stars and the CS cores is between 7″ and 24″(0.1 pc to 0.45 pc, in terms of physical distances), with the exception of G70.29+1.60, for which the separation is below 1″ (i.e., below 8000 AU). If the detected near-IR massive stellar population is contributing to the heating and stirring up (e.g., because of stellar winds) of the CS cores, one may expect some correlation between the near-IR spectral type and the brightness and velocity dispersion of the CS emission. We do not find such a correlation. The brightest CS core, with a mean beam temperature (T_{mb}) of 5.6 K (Bronfman et al. 1996), is associated with G5.89−0.39. However, this dense core is rather far away (∼0.3 pc) from the main near-IR ionizing star (and also from the radio-peak of the UC H II region). In contrast, the near-IR ionizing star(s) of G70.29+1.60, whose associated CS core has a relatively low T_{mb} (1.95 K), are coincident with the centroid of the CS emission. We note that the two cores with the broader CS(2−1) profiles are associated with G5.89−0.39 and G70.29+1.60, which are known to be strong outflow sources.

We also made an attempt to correlate the properties of the *MSX* sources associated with the UC H II regions in our sample, and the near-IR population. Inspection of our images shows that the centers of the *MSX* peaks are closer to the location of the radio UC H II regions than the CS cores and *IRAS* sources. In column (9) of Table 5, we show the luminosity associated with the *MSX* sources. This luminosity was calculated by integrating a blackbody fit using only the fluxes at 14.65 and 21.34 μm (see § 3.3), respectively. We find no correlation between the luminosity of the *MSX* source and the luminosity of the near-IR ionizing population.

4.2.6. *Possible Supergiants?*

We note that in three of the regions (G309.92+0.48, G61.48+0.09B1, and G70.29+1.60) the most luminous identified sources have near-IR colors consistent with being supergiants, rather than dwarfs. In the case of the regions G309.92+0.48 and G61.48+0.09B1, these stars appear to have spectral types early enough as to be responsible for the ionization of the H II region. A caveat should be pointed out here, since these high-luminosity sources may as well be mere unresolved ionized knots externally illuminated by other stars, rather than actual stars. Note that, for instance, an ionized knot emitting purely in Brγ may appear as a continuum source in the broadband K_s filter. If they are actually stars, their large absolute magnitude in the K band (M_K) would be likely to be generated by a single star, since it cannot be explained as due to an unresolved multiple system formed by two or more stars. To prove this, we analyze the most extreme case, i.e., two O3 V stars being misinterpreted as an O9.5 I star. The visual magnitude (M_v) and intrinsic colors for an O9.5 I star and an O3 V star are such that M_K(O9.5 I) = −5.65 mag and M_K(O3 V) = −4.79 mag, respectively (Vacca et al. 1996; Aller et al. 1982). An unresolved binary composed of two O3 V stars would have a total $M_K = −5.24$ mag, which is still 0.4 mag fainter than an O9.5 I star. This difference is larger than the typical error in our photometry. Nevertheless, this argument cannot be used to discard possible triple and multiple systems of dwarfs. In one particular case (G61.48+0.09) further Brγ and L' imaging strongly supports the interpretation of the most luminous

source being a supergiant rather than a dwarf (Puga et al. 2004).

Although further near-IR spectroscopy is required to confirm the nature of these high-luminosity sources (Kaper et al. 2002), we can argue whether, in terms of evolution, the presence of a supergiant in these H II regions is plausible. We use equation (9) from Wood & Churchwell (1989), with a typical value for the initial radius of the Strömgren sphere of 0.02 pc and a typical sound speed of 10 km s^{-1}. If we take into account the physical radii of G61.48+0.09B1, G70.29+1.60, and G309.92+0.48, i.e., 0.18, 0.14, and 0.03 pc, respectively, then the ages of these H II regions are 5×10^4, 2.5×10^4, and 1.1×10^3 yr, respectively.

This is between 2 and 3 orders of magnitude shorter than the typical time of $\lesssim 10^6$ yr required for a 40 $M_\odot$ star to reach the supergiant phase (Schaerer & de Koter 1997).

Several arguments can be used to reconcile the presence of supergiants in some of the UC H II regions. One may think that these luminous stars do not belong to the UC H II region, but that they are foreground stars situated at the position of the radio peak by chance alignments. This is rather unlikely though, since they tend to be the most embedded sources in our C-C diagram. Besides, even though our sample is rather small, we find possible ionizing supergiants in 25% of the cases, which is difficult to explain simply by chance alignments. The presence of supergiants could be explained if the H II regions were actually in a more advanced evolutionary stage than what is inferred from their physical size. This may be the case if radio single-beam observations (or low-resolution interferometry) of the ionized gas showed the presence of extended halos associated with these UC H II regions. However, in instances as G61.48+0.09, even with a low-resolution configuration of the VLA, the 3.6 cm emission extends only for 0.18 pc. The external pressure due to the molecular cloud in which UC H II regions are normally embedded may delay the expansion of the ionization front, yielding also older ages than what is predicted by simple expansion models. This argument has already been used before to explain the paradigm of the UC H II regions lifetime (Wood & Churchwell 1989). Tan & McKee (2004) show that an H II region will expand to a given size in a timescale 2 orders of magnitude slower in a clumpy turbulent medium than in a uniform medium.

5. CONCLUSIONS

We have analyzed AO-assisted J, H, and K/K' band images and photometry of eight UC H II regions. These data show details of the near-IR morphology and stellar population in these regions with unprecedented spatial resolution. We have analyzed the stellar population using near-IR photometry. We find that the typical spectral types obtained from near-IR photometry are earlier than those predicted from radio-continuum interferometric data available in the literature. The possible underestimate of the rate of Lyman photons from radio data due to absorption by dust, optical depth effects, clumpiness or the presence of undetected extended ionized halos may be causing this difference. We have also compared the ionizing and luminous near-IR stellar population with the luminosity of the *IRAS* source associated with each UC H II region. In general, we find that *IRAS* fluxes yield later spectral types for the dust heating source than near-IR photometry. This may be due to the presence of a more embedded stellar population than the one accessible with near-IR photometry. This hidden population would be the main contributor to the *IRAS* luminosity. Alternatively, if the dust distribution is anisotropic, the stars seen in the near-IR may actually be heating the dust seen by *IRAS*. Stellar models with spherical geometry and a detailed treatment of stellar winds and line blanketing yield radio- and *IRAS*-based spectral types that are generally in better agreement with photometry-based spectral types than non-LTE, plane-parallel models.

In all cases, the C-C diagrams for these regions show two groups of stars. We assume that one of them, close to the unreddened theoretical main sequence, is formed by foreground stars. The stars in the other one normally show a large spread in extinction, and they are certainly associated with the UC H II region. In all regions, we find at least one source with a spectral type early enough to be the ionizing star of the H II region, i.e., early B/O. We have counted, in spectral-type bins, all stars associated with each UC H II region. For G18.15−0.28, where we have a relatively high number of stars, a reasonable agreement is found between the observed O and B star numbers and those predicted by the IMF given in Miller & Scalo (1979). However, this is not the case for G61.48+0.09 and G70.29+1.60. For the remaining UC H II regions, not enough stellar counts were available to make any estimate.

We have also compared the luminosity of the near-IR ionizing stellar population with *MSX* luminosities and no correlation was found. Our near-IR data were compared with available millimeter CS data to find out what is the impact the massive stellar population in UC H II regions has on the surrounding dense gas. No correlation was found between the brightness of the CS emission and the luminosity of the best near-IR candidates to ionize the UC H II region. We note that the velocity dispersion is larger in the CS cores in the G5.89−0.39 and G77.96−0.01 regions, which are known to be associated with massive outflows.

In three regions (G61.48+0.09B1, G70.29+1.60, and G309.92+0.48), the most luminous stars in the UC H II region appear to be supergiants. In G61.48+0.09B1 and G309.92+0.48, these luminous stars are also the best candidates for ionizing sources of the H II region.

The main conclusion from this work is that AO-assisted near-IR imaging of UC H II regions with 4 m class telescopes is a useful tool to study the stellar population in massive star-forming regions. This appears to be a more accurate method to study the massive young stellar population than any indirect method based on radio, *IRAS*, or *MSX* measurements, mainly because of the higher resolution provided by AO observations. Nevertheless, it is also fundamental to observe at longer wavelengths (from 3.5 to 20 μm) with similar spatial resolution in order to detect the most embedded stellar population. Deeper observations are necessary to achieve a better coverage of the IMF. Finally, broadband imaging should be complemented with near-IR spectroscopy and narrowband imaging to fully understand the nature of the relevant stellar population in each region. AO imaging at 8 m class telescopes is a promising tool to achieve these goals.

ALVAREZ ET AL.

REFERENCES

Acord, J. M., Walmsley, C. M., & Churchwell, E. 1997, ApJ, 475, 693
Afflerbach, A., et al. 1996, ApJS, 106, 423
Aller, L. H., et al. 1982, Landolt-Börnstein: Numerical Data and Functional Relationships in Science and Technology, 451
Argon, A. L., Reid, M. J., & Menten, K. M. 2000, ApJS, 129, 159
Behrend, R., & Maeder, A. 2001, A&A, 373, 190
Beuzit, J., et al. 1994, Proc. SPIE, 2201, 955
Blair, G. N., Peters, W. L. & van den Bout, P. A. 1975, ApJ, 200, L161
Blitz, L., Fich, M., & Stark, A. A. 1982, ApJS, 49, 183
Bohlin, R. C., Savage, B. D., & Drake, J. F. 1978, ApJ, 224, 132
Bonnell, I. A., Bate, M. R., & Zinnecker, H. 1998, MNRAS, 298, 93
Braz, M. A., & Epchtein, N. 1983, A&AS, 54, 167
Bronfman, L., Nyman, L.-A., & May, J. 1996, A&AS, 115, 81
Burton, M. G., et al. 2000, ApJ, 542, 359
Cesaroni, R., et al. 1991, A&A, 252, 278
Churchwell, E., et al. 1978, A&A, 70, 719
Crowther, P. A., & Dessart, L. 1998, MNRAS, 296, 622
Cutri, R. M., et al. 2003, 2MASS All-Sky Catalog of Point Sources, VizieR, II/246
Deharveng, L., et al. 2000, A&A, 360, 1107
DePree, C. G., et al. 1994, ApJ, 428, 670
Ducati, J. R., Bevilacqua, C. M., Rembold, S. B., & Ribeiro, D. 2001, ApJ, 558, 309
Egan, M. P., et al. 2003, MSX6C Infrared Point Source Catalog, VizieR, V/114
Epchtein, N., & Lepine, J. R. D. 1981, A&A, 99, 210
Epchtein, N., et al. 1981, A&A, 97, 1
Evans, N. J., et al. 1981, ApJ, 250, 200
Feldt, M., Stecklum, B., Henning, Th., Hayward, T. L., Lehmann, T., & Klein, R. 1998, A&A, 339, 759
Feldt, M., et al. 1999, A&A, 346, 243
———. 2003, ApJ, 599, L91
Felli, M., & Harten, R. H. 1981, A&A, 100, 42
White, G. J., & Fridlund, C. V. M. 1992, A&A, 266, 452
Garay, G., Lizano, S., & Gomez, Y. 1994, ApJ, 429, 268
Garay, G., Rodriguez, L. F., Moran, J. M., & Churchwell, E. 1993, ApJ, 418, 368
Garay, G., et al. 1998a, ApJ, 501, 699
———. 1998b, ApJ, 501, 710
Harvey, P. M., & Forveille, T. 1988, A&A, 197, L19
Harvey, P. M., & Gatley, I. 1983, ApJ, 269, 613
Harvey, P. M., & Wilking, B. A. 1984, ApJ, 280, L19
Harvey, P. M., et al. 1994, ApJ, 433, 187
Henning, Th., Feldt, M., Stecklum, B., & Klein, R. 2001, A&A, 370, 100
Henning, Th., Pfau, W., & Altenhoff, W. J. 1990, A&A, 227, 542
Henning, Th., Stecklum, B., & Feldt, M. 2002, in ASP Conf. Ser. 267, Hot Star Workshop III: The Earliest Stages of Massive Star Birth, ed. P. A. Crowther (San Francisco: ASP), 153
Hillier, D. J., & Miller, D. L. 1998, ApJ, 496, 407
Hippler, S., Glindemann, A., & Kasper, M. 1998, Proc. SPIE, 3353, 44
Hofmann, K., Balega, Y., Preibisch, T., & Weigelt, G. 2004, A&A, 417, 981
Hofmann, R., Brandl, B., Eckart, A., Eisenhauer, F., & Tacconi-Garman, L. E. 1995, Proc. SPIE, 2475, 192
Hofner, P., & Churchwell, E. 1996, A&AS, 120, 283
Howard, E. M., et al. 1996, ApJ, 460, 744

Jackson, J. M., & Kraemer, K. E. 1999, ApJ, 512, 260
Kaper, L., Bik, A., Hanson, M. M., & Comerón, F. 2002, in ASP Conf. Ser. 267, Hot Star Workshop III: The Earliest Stages of Massive Star Birth, ed. P. A. Crowther (San Francisco: ASP), 95
Kim, K., & Koo, B. 2001, ApJ, 549, 979
Kurtz, S., Churchwell, E., & Wood, D. O. S. 1994, ApJS, 91, 659
Kurtz, S. E., et al. 1999, ApJ, 514, 232
Lenzen, R., Bizenberger, P., Salm, N., & Storz, C. 1998, Proc. SPIE, 3354, 493
Lockman, F. J. 1989, ApJS, 71, 469
Loughran, L., et al. 1986, ApJ, 303, 629
Martín-Hernández, N. L., et al. 2002, A&A, 381, 606
Martins, F., Schaerer, D., & Hillier, D. J. 2002, A&A, 382, 999
McBreen, B., et al. 1979, ApJ, 232, L183
McKee, C. F., & Tan, J. C. 2002, Nature, 416, 59
Miller, G. E., & Scalo, J. M. 1979, ApJS, 41, 513
Mokiem, M. R., Martín-Hernández, N. L., Lenorzer, A., de Koter, A., & Tielens, A. G. G. M. 2004, A&A, 419, 319
Nakano, T., Hasegawa, T., Morino, J., & Yamashita, T. 2000, ApJ, 534, 976
Okamoto, Y., et al. 2003, ApJ, 584, 368
Panagia, N. 1973, AJ, 78, 929
Pauldrach, A. W. A., Hoffmann, T. L., & Lennon, M. 2001, A&A, 375, 161
Peeters, E., et al. 2002, A&A, 381, 571
Phillips, J. P., & Mampaso, A. 1991, A&AS, 88, 189
Puga, E., et al. 2004, A&A, in press
Rengarajan, T. N., & Ho, P. T. P. 1996, ApJ, 465, 363
Roelfsema, P. R., Goss, W. M., & Geballe, T. R. 1988, A&A, 207, 132
Rubin, R. H., & Turner, B. E. 1969, ApJ, 157, L41
Simon, T., et al. 1985, MNRAS, 212, P21
Smith, L. J., Norris, R. P. F., & Crowther, P. A. 2002, MNRAS, 337, 1309
Schaerer, D., & de Koter, A. 1997, A&A, 322, 598
Schwartz, P. R., Wilson, W. J., & Epstein, E. E. 1973, ApJ, 186, 529
Shepherd, D. S., & Churchwell, E. 1996, ApJ, 457, 267
Sollins, P. K., et al. 2004, ApJ, in press (astro-ph/0403524)
Solomon, P. M., et al. 1987, ApJ, 319, 730
Straw, S. M., Hyland, A. R., & McGregor, P. J. 1989, ApJS, 69, 99
Tan, J. C., & McKee, C. F. 2004, in Cancun Workshop on Formation and Evolution of Young Massive Clusters, ed. H. Lamers, A. Nota, & L. Smith, in press (astro-ph/0403498)
Tokunaga, A. T. 2000, Allen's Astrophysical Quantities, ed. A. N. Cox (4th ed.; New York: AIP), 143
Turner, B. E., & Matthews, H. E. 1984, ApJ, 277, 164
Vacca, W. D., Garmany, C. D., & Shull, J. M. 1996, ApJ, 460, 914
Walsh, A. J., Hyland, A. R., & Robinson, G. 1997, MNRAS, 291, 261
Walsh, A. J., et al. 1998, MNRAS, 301, 640
———. 1999, MNRAS, 309, 905
Wink, J. E., Willson, T. L., & Bieging, J. H. 1983, A&A, 127, 211
Wolfire, M. G., & Cassinelli, J. P. 1987, ApJ, 319, 850
Wood, D. O. S., & Churchwell, E. 1989, ApJS, 69, 831
Wouterloot, J. G. A., & Brand, J. 1989, A&AS, 80, 149
Wynn-Williams, C. G., et al. 1977, ApJ, 342, 860
Yorke, H. W., & Sonnhalter, C. 2002, ApJ, 569, 846